PHYSICAL REVIEW RESEARCH **6**, 013277 (2024)

Localized source above a time-modulated dielectric half-space: Green's function theory

Michael Kreiczer,[1] Ben Z. Steinberg,[1] and Yakir Hadad[1,2,*]
[1]*The School of Electrical Engineering, Tel-Aviv University, Ramat-Aviv, Tel-Aviv 69978, Israel*
[2]*Center for Light-Matter Interaction, Tel-Aviv University, Tel-Aviv 67798, Israel*

(Received 29 November 2023; revised 1 February 2024; accepted 7 February 2024; published 13 March 2024)

In this paper, we explore the two-dimensional Green's function problem above an instantaneous time-modulated dielectric half-space. In particular, we focus on studying the excitation dynamic with modulation that is carried out near the critical angle and the total internal reflection regime, where an impinging spectrum of waves expects the so-called lateral wave excitation on the interface. We start by analyzing the reflection of a plane wave, with detailed attention given to the difference between two cases: a slow quasistatic modulation versus a relatively fast modulation that leads to substantial excitation of intermodulation frequencies. Next, we provide a space-time *spectral* representation to the space-domain Green's function, and later, we move to evaluate the spectral integral both in a brute-force numerically exact manner and using integration along the steepest descent path and the branch cuts, which unravel the distinction between different wave phenomena associated with the excitation problem. Thus, we identify different wave species that can be associated with reflected rays and waves that resemble the known head wave in the classical problem of stationary stratified media. We examine the unique time-dependent behavior of each wave species that arises as a consequence of the interface between the time-harmonics of the reflected space-time plane wave spectrum. Lastly, we demonstrate the broader validity of our analytical predictions, also in the case of a dispersive and finite time-modulated medium. To that end, we use a full-wave simulation of a source above a finite time-modulated thick layer that is implemented using a time-varying wire medium. These full-wave results are compared with our current analytical model with effective (homogenized) parameters of the time-modulated wire medium taken from Phys. Rev. Appl. **16**, 054003 (2021).

DOI: 10.1103/PhysRevResearch.6.013277

I. INTRODUCTION

The study of electromagnetic wave dynamics in time-varying media goes back several decades [1,2]. The benefits of removing the restriction caused by time invariance, and adding another dimension for engineering-time, has opened a whole new area of technological possibilities. Recently, there has been a renewed interest in research in this direction, especially in the context of new developments for the next generation in the research of metamaterials, for applications such as inverse prism functionality, frequency conversions, temporal band gap, magnetless nonreciprocity, time reversal, and effective permittivity realization by temporal switching [3–36] including devices that outperform physical linear and time-invariant (LTI) bounds [37–42]. One major analysis aspect of temporal metastructures, that so far has been only marginally explored, is their excitation mechanism. Recently, a study of the excitation mechanism for a spatiotemporal metasurface has been presented [43]. The emphasis of this study was the rigorous development of the spectral representation of the space-domain Green's function and the physical interpretation of the singular and critical points in the complex plane of the spectral variable.

In this paper, we expand the study of the excitation mechanism to the canonical problem of time-modulated dielectric half-space (see Fig. 1). To that end, we specifically choose to focus on the excitation problem of a semi-infinite time-modulated instantaneous (nondispersive) dielectric half-space by a localized two-dimensional source. We study and develop rigorously the spectral representation of the space-domain Green's function and the physical interpretation of the singular and critical points in the complex plane of the spectral variable. Using this study, we explore the unique time-dependent behavior of each wave species that arises as a consequence of the interface between the time-harmonics of the reflected space-time plane wave spectrum. One of the challenges when analyzing discontinuity between two materials and seeking close analytical expressions is performing the mode matching effectively. Thus, we limit ourselves in this paper to weak modulation in time.

A time-varying medium can be achieved in various approaches. The first prominent one is using exotic materials such as semiconductors whose permittivity can be tuned by the field effect, or by nonlinear materials whose polarization response can be biased by high-intensity optical pumping. The second approach is to use time-variant artificial (composite) media, as described in detail in [16], for the case of a spatiotemporally modulated wire medium [44–60]. Here the emphasis of the study is given to the behavior in the time domain of the reflected field, with a detailed examination of the

---

[*] hadady@eng.tau.ac.il

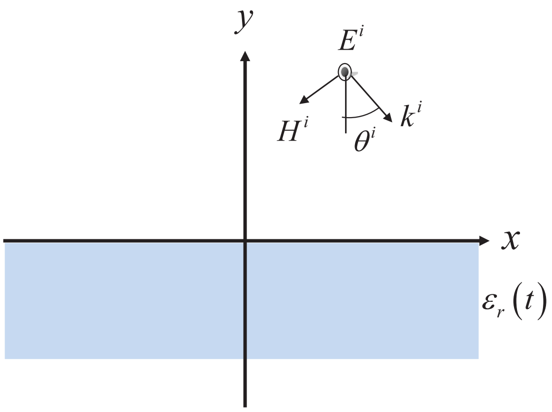

FIG. 1. The problem setup. The lower half-space consists of a time-varying dielectric. The upper half-space is a vacuum. The source is located in the vacuum.

effect of the critical points for both the nominal frequency and the close harmonics in the complex spectral plane, and separation between a specular ray due to a saddle point contribution, and a head-wave-like wave that corresponds to the branch point singularities. To analyze the time-variant discontinuity excitation dynamics, we take a bottom-up approach. We first define the time-variant susceptibility and use Maxwell's equation to calculate the eigenmodes of the time-varying medium. To that end, we follow the approach described in [16]. Those eigenmodes let us perform the mode-matching calculation at the spatial boundary, and get a closed-form approximate expression for the reflected field coefficients for an incident plane wave. This result is consequently used to construct the Green's function of the problem as a space-time spectral integral. Later, we study the singular and critical points in the complex spectral plane and use them to identify different waves and phenomena in the system both in the frequency domain and the time domain. Lastly, we compare our analytic results with full-wave simulations carried out for a time-varying finite wire medium.

The paper is organized as follows. In Sec. II, we define the physical time-variant configuration we study, and we calculate the eigenmodes for both slow quasistatic modulation and fast modulation. Then, in Sec. III we derive the reflection coefficients for an incident plane wave. This is carried out using analytical approximations and by a brute-force numerical calculation. We emphasize the differences between slow quasistatic modulation and relatively fast modulation. Based on the derivations in the previous sections, in Sec. IV we construct the Green's function of a two-dimensional (2D) line source above a time-modulated half-space as a spectral integral, and we explore the physical interpretation of the singular and critical points in the complex spectral plane. Finally, in Sec. V we implement a homogenization technique [16] for the case of a time-modulated half-space wire medium, and we compare our analysis with brute-force numerical simulations.

II. TEMPORALLY MODULATED DIELECTRIC MEDIUM

Our goal in this paper is to explore the 2D Green's function problem above a temporally modulated dielectric discontinuity. As a basic building block, we begin with the scattering problem due to a single monochromatic plane wave incidence. Our analysis is based on the concept of harmonic balance, which can be regarded as a quasifrequency domain (QFD) technique. We start with the analysis of the eigenmodes of a modulated dielectric medium. The relation between the electric field and the electric displacement in the time domain can be written as

$$\vec{D}(t) = \varepsilon_0\vec{E}(t) + \vec{P}(t), \tag{1}$$

where $\vec{P}(t)$ is the polarization density vector. We assume that the medium is linear, i.e., the fields are weak enough so that the polarization and the field are connected through a linear operation. In this case, the polarization relates to the electric field via the impulse response of the medium $f(t,\tau)$,

$$\vec{P}(t) = \varepsilon_0\int_{-\infty}^{\infty} f(t,\tau)\vec{E}(\tau)d\tau. \tag{2}$$

We limit our analysis to the case of an instantaneous response of the medium. In this case, for an impulse input of $\delta(t-\tau)$, the response will be $a(\tau)\delta(t-\tau)$. Using this impulse response, we can now write the polarization using superposition,

$$\vec{P}(t) = \varepsilon_0\int_{-\infty}^{\infty} a(\tau)\delta(t-\tau)\vec{E}(\tau)d\tau = \varepsilon_0 a(t)\vec{E}(t). \tag{3}$$

Let us now assume a small harmonic perturbation of the medium, in the form of $a(t) = \chi_0(1 + m\cos\Omega t)$. χ_0 is the electric susceptibility of the unperturbed medium, which satisfied $\varepsilon_{r0} = \chi_0 + 1$, with ε_{r0} the permittivity of the unperturbed medium. We get the following relation for the electric displacement field:

$$\vec{D}(t) = \varepsilon_0[1 + (\varepsilon_{r0} - 1)(1 + m\cos\Omega t)]\vec{E}(t) \tag{4}$$

with $m \ll 1$. For the sake of simplicity, we limit ourselves to the 2D case and a $\hat{z}$ polarized electric field, i.e., the TE mode. With Ampere's law,

$$\vec{\nabla}\times\vec{H}(t) = \hat{z}\frac{d}{dt}\{\varepsilon_0[1 + (\varepsilon_{r0} - 1)(1 + m\cos\Omega t)]E(t)\}, \tag{5}$$

we can use the Fourier transform, and get the relation between the electric and magnetic fields in the frequency domain. We can now get the expected recursive relation between the fields, which allows us to use the harmonic balance technique, and follow the method previously developed in [16],

$$\vec{\nabla}\times\vec{H}(\omega) = j\hat{z}\omega\varepsilon_0\left\{\begin{matrix}\varepsilon_{r0}E(\omega)+\\ \frac{m}{2}(\varepsilon_{r0}-1)[E(\omega+\Omega)+E(\omega-\Omega)]\end{matrix}\right\}. \tag{6}$$

We can write the electric and magnetic fields in the following way:

$$E(\omega) = \sum_{n=-\infty}^{\infty} E_n\delta(\omega-\omega_n), \tag{7a}$$

$$H(\omega) = \sum_{n=-\infty}^{\infty} H_n\delta(\omega-\omega_n), \tag{7b}$$

where $\omega_n = \omega_0 + n\Omega$. We can now get the following relation between the time-harmonics of the electric field (see Appendix A),

$$\left(q^2 - \varepsilon_{r0} k_n^2\right) E_n = \frac{m k_n^2}{2} (\varepsilon_{r0} - 1)(E_{n-1} + E_{n+1}). \tag{8}$$

The recursive relation in Eq. (8) can now be represented using a tridiagonal matrix of an infinite rank,

$$\underline{\underline{A}}\,\underline{E} = 0, \tag{9}$$

where

$$\underline{\underline{A}} = \begin{bmatrix} \ddots & \ddots & 0 & 0 & & & \\ \ddots & b_{-2} & c_{-2} & 0 & 0 & & \\ 0 & a_{-1} & b_{-1} & c_{-1} & 0 & 0 & \\ 0 & 0 & a_0 & b_0 & c_0 & 0 & 0 \\ & 0 & 0 & a_1 & b_1 & c_1 & 0 \\ & & 0 & 0 & a_2 & b_2 & \ddots \\ & & & 0 & 0 & \ddots & \ddots \end{bmatrix} \tag{10a}$$

and

$$\underline{E} = [\dots, E_{-N}, E_{-N+1}, \dots, E_N, \dots]^T. \tag{10b}$$

The matrix entries a_n, b_n, c_n are

$$a_n = -\tfrac{1}{2} m k_n^2 (\varepsilon_{r0} - 1), \tag{11a}$$

$$b_n = q^2 - \varepsilon_{r0} k_n^2, \tag{11b}$$

$$c_n = a_n. \tag{11c}$$

The eigenmodes can be found by nullifying the determinant

$$|\underline{\underline{A}}| = 0. \tag{12}$$

The matrix in Eq. (10a) can be truncated to a finite size when a_n, c_n are much smaller than the diagonal elements b_n. We mark the truncated matrix with $\underline{\underline{A}}^{\{N\}}$—this matrix has $2N + 1$ rows and columns. Since in our case $m \ll 1$, this approximation is valid when the eigenmodes are not too close to each other. When solving the equation that arises from Eq. (12), for a finite size $2N + 1$ matrix, we get a $2(2N + 1)$ solution for the eigenmodes q. Since we are interested only in plane waves propagating away from the discontinuity, we need to take into consideration only $2N + 1$ eigenmodes with positive q—we mark those eigenmodes with $q^{(s)}$, $s = -N, -N + 1, \dots, N - 1, N$. We separate our analysis into two different cases:

(i) Case I: Slow quasistatic modulation, i.e.,

$$O\left(\frac{\Omega}{\omega}\right) \ll O(m^2). \tag{13}$$

(ii) Case II: Fast modulation, i.e.,

$$O\left(\frac{\Omega}{\omega}\right) \gg O(m^2). \tag{14}$$

We elaborate on these two cases in the following sections.

A. Case I: Slow (quasistatic) modulation

We start with the analysis of case I—the slow modulation. In this case, we assume a very slow modulation, which allows us to completely neglect $\frac{\Omega}{\omega}$ (see Appendix B). The matrix elements in Eq. (10a) can be approximated to be independent of n, given specifically by

$$a = -\tfrac{1}{2} m (\varepsilon_{r0} - 1) k_0^2, \tag{15a}$$

$$b = q^2 - \varepsilon_{r0} k_0^2. \tag{15b}$$

The resulting tridiagonal matrix in Eq. (10a) becomes a Toeplitz matrix [61]. Assuming that the infinite rank matrix is truncated into a $2N + 1$ square matrix for the $2N + 1$ first harmonics of the field $E_{-N}, \dots, E_N$, then a closed form expression for its eigenvalues exists: $\lambda = b + 2a \cos \frac{s\pi}{2(N+1)}$, with $s = 1, \dots, 2N + 1$. In our case, λ stands for q^2. We get the eigenmode expression (as mentioned before, we only use the positive eigenvalues). In the result, we use the approximation for $m \ll 1$, and we write the expression in a symmetrical form ($s = 0$ represents the regular mode),

$$q^{(s)} \approx \sqrt{\varepsilon_{r0}} k_0 \left[1 - \frac{1}{2} \frac{|\varepsilon_{r0} - 1|}{\varepsilon_{r0}} m \cos\left(\frac{(s + N + 1)\pi}{2N + 2}\right)\right],$$
$$s = -N, \dots, N. \tag{16}$$

This analytic solution for the eigenvalues reveals a very dominant dependence on the actual matrix size, N. This could already be observed by the fact that $O(b) = O(a) = O(m)$, which eliminates the possibility of truncating the matrix in Eq. (10a) to a small size matrix, even for small m. The unavoidable conclusion from the analysis of the quasistatic slow modulation is that one cannot easily construct the electromagnetic field using a relatively small eigenvector dimension. It seems that the spectrum of the slow-medium case is close to continuous, and it is therefore significantly more challenging to analyze using modal decomposition and a quasifrequency domain approach. However, since the modulation in this case is so slow compared with the impinging wave frequency, the problem may be considered adiabatic for most practical cases. Thus the time variable in the time-modulated susceptibility can be treated as a parameter, as discussed in Sec. III C below.

B. Case II: Fast modulation

We can now move to the somewhat more interesting Case II—the fast modulation. We emphasize that here the modulation is slower compared with the impinging wave frequency, however it is not extremely small as is required to satisfy the slow modulation condition that is stated in Eq. (13) above. Instead here we assume that Eq. (14) is satisfied. In this case, we can follow the approach developed in [16], and truncate the infinite matrix in Eq. (10a) to a 3×3 matrix to ease our calculating of the eigenmodes. This $N = 1$ matrix approximation is given in Eq. (17),

$$\begin{pmatrix} b_{-1} & c_{-1} & 0 \\ a_0 & b_0 & c_0 \\ 0 & a_1 & b_1 \end{pmatrix} \begin{pmatrix} E_{-1} \\ E_0 \\ E_1 \end{pmatrix} = 0. \tag{17}$$

In this case, the determinant reduces to

$$\frac{a_0 c_{-1}}{b_{-1}} + \frac{a_1 c_0}{b_1} \approx b_0. \tag{18}$$

By substituting the expressions for a_n, b_n, c_n in Eq. (11), we get

$$\frac{m^2(\varepsilon_{r0}-1)^2 k_0^2 k_{-1}^2}{4\left(q^2-\varepsilon_{r0}k_{-1}^2\right)} + \frac{m^2(\varepsilon_{r0}-1)^2 k_0^2 k_1^2}{4\left(q^2-\varepsilon_{r0}k_1^2\right)} = q^2 - \varepsilon_{r0}k_0^2. \tag{19}$$

For the case of a 3×3 matrix, we get three positive eigen-wave-numbers $q^{(s)}$ with $s = -1, 0, 1$. The regular mode $q^{(0)}$ represents the mode of the unperturbed medium, i.e., the mode of the stationary case, and $q^{(-1)}, q^{(1)}$ represent the irregular modes (i.e., waves that are excited due to the time-modulation). We start with the regular mode $q^{(0)}$. Obviously for $m = 0$ the regular mode satisfies $q(m = 0) = \sqrt{\varepsilon_{r0}}k_0$. We can approximate the small bias from the unmodulated solution (since $m \ll 1$) by substituting $q(m = 0)$ on the left-hand side (LHS) of Eq. (19). We get

$$q^{(0)} \approx \sqrt{\varepsilon_{r0}}k_0\left[1 + \frac{\tilde{m}^2}{8}\left(\frac{k_{-1}^2}{k_0^2-k_{-1}^2} + \frac{k_1^2}{k_0^2-k_1^2}\right)\right], \tag{20}$$

where we define

$$\tilde{m} = m\frac{\varepsilon_{r0}-1}{\varepsilon_{r0}}. \tag{21}$$

For the irregular modes, we assume that since the two expressions on the LHS of Eq. (19) increase rapidly for a different q, and since both numerators are is small, we can approximate the eigen-wave-numbers to be close to the values that nullify the denominators. We also notice the numerators on the LHS are of order $O(m^2)$, while the denominators are of order $O(\frac{\Omega}{\omega})$, which lead us to the demand for this fast modulation analysis of $O(\frac{\Omega}{\omega}) \gg O(m^2)$. Again, as we did in the calculation for $q^{(0)}$, we substitute $q^{(1)}(m = 0) \approx \sqrt{\varepsilon_{r0}}k_1$ on the right-hand side (RHS) of Eq. (19), and also in the left element of the LHS. We note that the smaller the modulation amplitude m is, the harder it is to excite the irregular modes. We do the same for the $s = -1$ mode, by substituting $q^{(-1)}(m = 0) \approx \sqrt{\varepsilon_{r0}}k_{-1}$ on the RHS of Eq. (19) and the right expression of the LHS. This eventually leads to the following approximation:

$$q^{(s)} \approx \sqrt{\varepsilon_{r0}}k_s\left[1 + \frac{\tilde{m}^2 k_0^2}{8\left(k_s^2-k_0^2\right)}\right], \qquad s = \pm 1. \tag{22}$$

We note that unlike in [16], where we were satisfied with a less accurate approximation for those modes, here we aim to span the field, using the plane waves that correspond to these eigen-wave-numbers, and therefore we require a more accurate calculation to avoid artificial nonphysical singularities. To be specific, note that using the less accurate approximation of $q^{(\pm1)} \approx q^{(\pm1)}(m = 0)$ nullifies the matrix element $b_{\pm1}$, which makes it impossible to perform the following mode-matching calculation at the interface between the two half-spaces [see the discussion about Eqs. (42a) and (42b) below]. In Fig. 2 we compare the analytical approximations in Eqs. (20) and (22) to the numerical calculation via Eq. (12) both for $N = 1$ and 2 [the equation for $N = 1$ is also presented in Eq. (19)] for $\Omega/\omega^0 = 0.1$, $m = 0.2$, $\varepsilon_{r0} = 0.7$. We can see the dispersion relations for the wave numbers for each mode, and we notice that, unlike the slow modulation case, here the first three modes have almost no dependence on the truncation size N of the matrix, as demonstrated by the numerical calculation.

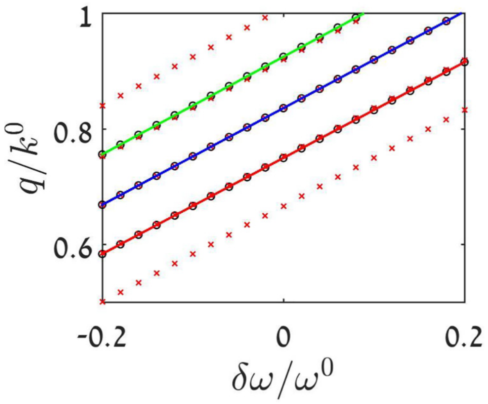

FIG. 2. Dispersion relation for the slow modulation case, as obtained by the expressions in Eqs. (20) and (22). The wave number q of each one of the solutions is shown as a function of the normalized frequency shift $\delta\omega/\omega_0$. Continuous lines represent the analytical results, circles represent the numerical results for $N = 1$, and an x mark represents the numerical results for $N = 2$. Here we see that the calculation of the first three modes has almost no dependence on N.

III. PLANE WAVE ILLUMINATION OF INFINITE HALF-SPACE

A. General expression

We can now examine the problem of scattering an illuminating plane wave by a time-modulated dielectric half-space. Consider a $\hat{z}$ polarized incident plane wave, as described in Fig. 1,

$$\vec{E}^{\text{inc}} = \hat{z}\tilde{E}^i e^{-j\vec{k}^i\cdot\vec{r}}. \tag{23}$$

At the interface between the two half-spaces, the tangential electric and magnetic fields are continuous. In our calculations, we use the positive eigenvalues from the previous section, since we are interested in temporal modes that propagate away from the discontinuity, in the positive y direction. We start with a general expression for a given N. For every temporal harmonic, the electric and magnetic fields that are transmitted into the time-variant medium can be written as a sum over the eigenmodes

$$\tilde{E}_n^t = \sum_{s=-N}^{N} \tilde{E}_n^{t,(s)}, \tag{24a}$$

$$\tilde{H}_n^t = \sum_{s=-N}^{N} \tilde{H}_n^{t,(s)}. \tag{24b}$$

The continuity demand for the electric field gives the following equations for every harmonic n:

$$\tilde{E}^i e^{-jk_x x}\delta_{n0} + \tilde{E}_n^r e^{-jk_x x} = \sum_{s=-N}^{N} \tilde{E}_n^{t,(s)} e^{-jq_x^{(s)}x} \tag{25}$$

with $k_x = k_0 \sin\theta^i$, and where the sum over the index s represents the summation over the modes of the transmitted field, and δ_{n0} is the Kronecker delta. Since the continuity needs to be valid for every x, we can omit the exponents in Eq. (25), and moreover write a generalized Snell's law [62],

$$k_0 \sin\theta^i = q^{(s)} \sin\theta^{t,(s)}, \tag{26}$$

where $\theta^{t,(s)}$ represents the angle of the transmitted field for the temporal mode with index s. We can see that every eigenmode has a different transmission angle. We also see that the reflecting angle equals the incident angle only for the nominal frequency $n = 0$,

$$k_0 \sin\theta^i = k_n \sin\theta_n^r. \tag{27}$$

The reduced expression for the electric fields gets the following simplified form:

$$-\tilde{E}_n^r + \sum_{s=-N}^{N} \tilde{E}_n^{t,(s)} = \tilde{E}^i \delta_{n0}. \tag{28}$$

We can now move to the magnetic field. Here we need to project the vector over the discontinuity surface. We get

$$\cos\theta_n^r \tilde{H}_n^r + \sum_{s=-N}^{N} \cos\theta^{t,(s)} \tilde{H}_n^{t,(s)} = -\cos\theta^i \tilde{H}^i \delta_{n0} \tag{29}$$

We use the following relation between the transmitted magnetic and electric fields (see Appendix A):

$$q^{(s)} \tilde{H}_n^{t,(s)} = \hat{z} j \varepsilon_0 \varepsilon_{r0} \omega_n \left[E_n + \frac{\tilde{m}}{2}(E_{n-1} + E_{n+1}) \right]. \tag{30}$$

We can now rewrite Eq. (29) in terms of the relation between the electric fields. To that end, for the transmitted field in the time-variant medium, we use Eq. (30), and for the incident and reflected fields we can simply use the free space relation $E_n^r = \eta H_n^r$, $E_n^i = \eta H_n^i$. We can now define new variables that represent the *effective wave velocity* perpendicular to the interface, in the vacuum, and in the time-variant medium for all time harmonics,

$$\xi_0^i = c \cos\theta^i, \tag{31a}$$

$$\xi_n^r = c \cos\theta_n^r, \tag{31b}$$

$$\xi_n^{t,(s)} = c\varepsilon_{r0} \frac{k_n}{q^{(s)}} \cos\theta^{t,(s)}, \tag{31c}$$

where c denotes the speed of light in vacuum. Thus we get the following recursive equation the time harmonics:

$$\xi_n^r \tilde{E}_n^r + \sum_{s=-N}^{N} \xi_n^{t,(s)} \left[\tilde{E}_n^{t,(s)} + \frac{\tilde{m}}{2}\left(\tilde{E}_{n-1}^{t,(s)} + \tilde{E}_{n+1}^{t,(s)}\right) \right] = \xi_0^i \tilde{E}^i \delta_{n0}. \tag{32}$$

The sets of equations in Eqs. (28) and (32) provide us with $2(2N+1)$ equations. However, the total of unknowns in our physical problem is $4N^2 + 6N + 2$. This number comes as follows: $2N+1$ are $\tilde{E}_n^r$ for every n, and $(2N+1)^2$ are $\tilde{E}_n^{t,(s)}$ for every n and s. To find additional $2N(2N+1)$ equations, we simply use the fact that every eigenmode of the transmitted field satisfies the field relation between the harmonics in Eq. (8). This gives us $2N(2N+1)$ as required and not $(2N+1)^2$ as one may argue since the demand is for the nullification of the determinant in Eq. (12), which states that the rows are linearly dependant. Let us define the matrix $\underline{\underline{A}}^{(s)}$. This $(2N)\times(2N+1)$ matrix represents the linearly independent rows of the matrix Eq. (10a) for the eigenmode with index s. To solve this set of linear equations, We define the following matrices:

$$\underline{\underline{U}} = \mathrm{diag}\left[\xi_{-N}^r, \ldots, \xi_0^r, \ldots, \xi_N^r\right] \tag{33}$$

and

$$\underline{\underline{T}}^{(s)} = \begin{bmatrix} \xi_{-N}^{t,(s)} & \frac{\tilde{m}}{2}\xi_{-N}^{t,(s)} & 0 & & & & \\ 0 & \ddots & \ddots & & & & \\ & \ddots & & & & & \\ & & \frac{\tilde{m}}{2}\xi_0^{t,(s)} & \xi_0^{t,(s)} & \frac{\tilde{m}}{2}\xi_0^{t,(s)} & & \\ & & & & & \ddots & \\ & & & & \ddots & \ddots & \\ & & & & & \frac{\tilde{m}}{2}\xi_N^{t,(s)} & \xi_N^{t,(s)} \end{bmatrix}. \tag{34}$$

We also define the following vectors:

$$\underline{v} = [0, 0, \ldots, 0, 1, 0, 0, \ldots, 0], \tag{35a}$$

$$\underline{\tilde{E}}^r = \left[\tilde{E}_{-N}^r, \ldots, \tilde{E}_{-1}^r, \tilde{E}_0^r, \tilde{E}_1^r, \ldots, \tilde{E}_N^r\right], \tag{35b}$$

$$\underline{\tilde{E}}^{t,(s)} = \left[\tilde{E}_{-N}^{t,(s)}, \ldots, \tilde{E}_{-1}^{t,(s)}, \tilde{E}_0^{t,(s)}, \tilde{E}_1^{t,(s)}, \ldots, \tilde{E}_N^{t,(s)}\right], \tag{35c}$$

We now define the large matrix $\underline{\underline{W}}$, which is assembled from the previously defined matrices, and represents the group of all the equations.

$$\underline{\underline{W}}=\begin{bmatrix} -\underline{\underline{I}} & \underline{\underline{I}} & \underline{\underline{I}} & \cdots & \underline{\underline{I}} & \underline{\underline{I}} & \underline{\underline{I}} \\ \underline{\underline{U}} & \underline{\underline{T}}^{(1)} & \underline{\underline{T}}^{(2)} & \cdots & \underline{\underline{T}}^{(2N-1)} & \underline{\underline{T}}^{(2N)} & \underline{\underline{T}}^{(2N+1)} \\ 0 & \underline{\underline{A}}^{(1)} & 0 & & & & \\ & 0 & \underline{\underline{A}}^{(2)} & 0 & & & \\ & & & & & & \\ & & & & & \ddots & 0 \\ & & & & & 0 & \underline{\underline{A}}^{(2N+1)} \end{bmatrix}. \tag{36}$$

The unknown variables vector and the excitation vector are expressed by concatenating the vectors defined in Eq. (35),

$$\underline{\tilde{E}}=[\underline{\tilde{E}}^{r},\underline{\tilde{E}}^{t,(-N)},\underline{\tilde{E}}^{t,(-N+1)},\dots,\underline{\tilde{E}}^{t,(N)}]^{T}, \tag{37a}$$

$$\underline{V}=\left[\tilde{E}^{i}\underline{v},\xi_{0}^{i}\tilde{E}^{i}\underline{v},0,\dots,0\right]^{T}. \tag{37b}$$

The solution will be

$$\underline{\tilde{E}}=\underline{\underline{W}}^{-1}\underline{V}. \tag{38}$$

In the following sections, we examine a plane wave illumination at the critical angle of the nominal stationary medium. We choose $\varepsilon_{r0}=0.7$, which leads to a critical angle of $\theta_{c}^{i}=0.99$ radians.

B. Illumination of a slow quasistatic modulation medium

In the case of a slow quasi-statically modulated medium, the frequencies of the temporal harmonics become very close to each other. Therefore, it is reasonable to approximate the discrete spectrum with a continuous one. Thus, we can simply start with the standard Fresnel coefficient, and add the time dependence in an adiabatic approach,

$$E^{r}=\frac{\cos\theta^{i}-\sqrt{\varepsilon_{r}(t)}\cos\theta^{t}(t)}{\cos\theta^{i}+\sqrt{\varepsilon_{r}(t)}\cos\theta^{t}(t)}, \tag{39}$$

where $\varepsilon_{r}(t)=1+(\varepsilon_{r0}-1)(1+m\cos\Omega t)$ and $\theta^{t}(t)=\arcsin\frac{k_{0}\sin\theta^{i}}{\sqrt{\varepsilon_{r}(t)}}$. In the time domain, we can write the approximate slow modulation calculation,

$$E^{r}(t)=\left|\frac{\cos\theta^{i}-\sqrt{\varepsilon_{r}(t)}\cos\theta^{t}(t)}{\cos\theta^{i}+\sqrt{\varepsilon_{r}(t)}\cos\theta^{t}(t)}\right| \times\cos\left(\omega_{0}t+\angle\frac{\cos\theta^{i}-\sqrt{\varepsilon_{r}(t)}\cos\theta^{t}(t)}{\cos\theta^{i}+\sqrt{\varepsilon_{r}(t)}\cos\theta^{t}(t)}\right). \tag{40}$$

For the case of slow modulation with $\Omega/\omega^{0}=0.01$, in Fig. 3 we show the reflected field in the time domain ($T=2\pi/\Omega$) for incidence at the critical angle of the nominal corresponding stationary medium. As expected, we get total reflection for half a cycle of the slow modulation, whereas, for the other half, we get regular reflected and transmitted plane waves.

C. Illumination of a fast modulated medium

As previously stated, the fast modulation case is the interesting one, and therefore the one we focus on for the rest of the paper. We aim to achieve a closed-form expression for the reflected field. To do so, we limit ourselves to the approximation of $N=1$. We start with the relation from Eq. (8), and we obtain

$$\tilde{E}_{1}^{t,(s)}=\psi_{1}^{(s)}\tilde{E}_{0}^{t,(s)}, \tag{41a}$$

$$\tilde{E}_{-1}^{t,(s)}=\psi_{-1}^{(s)}\tilde{E}_{0}^{t,(s)}, \tag{41b}$$

with

$$\psi_{1}^{(s)}=\frac{\tilde{m}\varepsilon_{r0}k_{1}k_{0}}{2\left((q^{(s)})^{2}-\varepsilon_{r0}k_{1}^{2}\right)}, \tag{42a}$$

$$\psi_{-1}^{(s)}=\frac{\tilde{m}\varepsilon_{r0}k_{-1}k_{0}}{2\left((q^{(s)})^{2}-\varepsilon_{r0}k_{-1}^{2}\right)}. \tag{42b}$$

When examining the denominator of Eqs. (42a) and (42b), we notice the need to use the correction in the calculation of the irregular modes in Eq. (22), to avoid artificial singularities. We can use the expressions for the eigenmode wave numbers $q^{(s)}$, and note that for ε_{r0} which is not too small [as we see in Eq. (21), when ε_{r0} is too small, the value of $\tilde{m}$ can be high, which leads to a reduction in the accuracy of this approximation], that $\psi_{1}^{(1)},\psi_{-1}^{(-1)}$ have larger absolute value than the rest—$\psi_{1}^{(1)},\psi_{-1}^{(-1)}=O(\frac{1}{\tilde{m}})$, where $\psi_{\pm1}^{(0)},\psi_{-1}^{(1)},\psi_{1}^{(-1)}=O(\tilde{m})$. We also expect a much stronger response for the regular mode than for the irregular modes, i.e., $|\tilde{E}_{0}^{t,(0)}|\gg|\tilde{E}_{0}^{t,(1)}|,|\tilde{E}_{0}^{t,(-1)}|$. Therefore, to ease the algebra, we can also use the assumption for a strong response for the regular mode, and neglect elements with $O(\tilde{m}E_{0}^{(s\neq0)})$. Under these considerations, with $N=1$ the linear system in Eq. (38) is 6×6 and can be solved

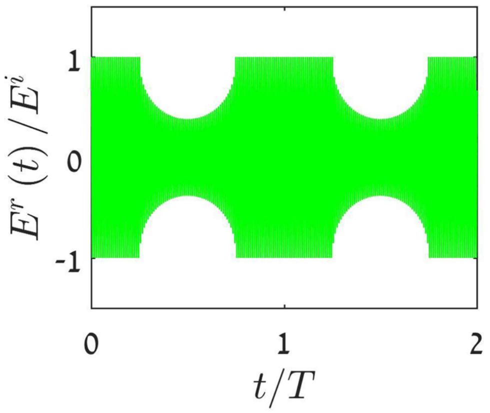

FIG. 3. Reflected fields for an incident plane wave at the critical angle, for the slow quasistatic modulation case. As expected, we get total reflection for half a cycle of the slow modulation, whereas for the other half we get regular reflected and transmitted plane waves.

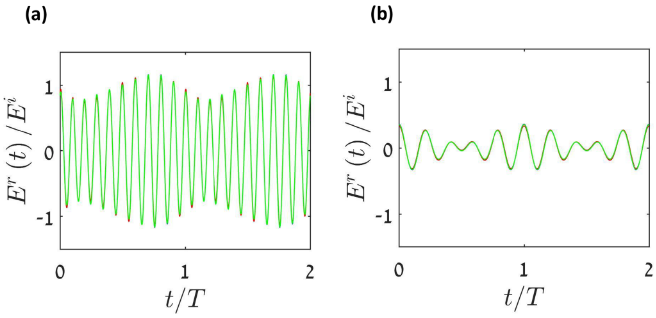

FIG. 4. Reflected fields for the fast modulation case. Blue, calculation with $N = 1$; red, calculation with $N = 2$; green, analytic approximation. (a) $\theta^i = \theta^i_c = 0.99$ rad and $\Omega/\omega^0 = 0.1$; (b) $\theta^i = 0.73$ rad and $\Omega/\omega^0 = 0.2$.

analytically for the reflected and transmitted electric field harmonics. Using this solution, we can write the expression for the reflection coefficients for the different time harmonics,

$$\Gamma_{\pm1} = 2\xi^i_0\big(\psi^{(0)}_{\pm1} - \psi^{(\pm1)}_{\pm1}C_{\pm1}\big)/D, \tag{43a}$$

$$\Gamma_0 = \frac{\xi^i_0 - \xi^{t,(0)}_0 - \big(\xi^i_0 - B_{+1}\big)C_{+1} - \big(\xi^i_0 - B_{-1}\big)C_{-1}}{D}, \tag{43b}$$

where $\Gamma_n = \frac{\tilde{E}^r_n}{\tilde{E}^i}$ on the interface, and

$$D = \xi^i_0 + \xi^{t,(0)}_0 - \big(\xi^i_0 + B_{+1}\big)C_{+1} - \big(\xi^i_0 + B_{-1}\big)C_{-1} \tag{44}$$

with

$$B_{\pm1} = \xi^{t,(\pm1)}_0 + \xi^{t,(\pm1)}_0 \frac{\tilde{m}}{2}\psi^{(\pm1)}_{\pm1}, \tag{45a}$$

$$C_{\pm1} = \frac{\xi^{t,(0)}_{\pm1}\psi^{(0)}_{\pm1} + \xi^{t,(0)}_{\pm1}\frac{\tilde{m}}{2} + \xi^r_{\pm1}\psi^{(0)}_{\pm1}}{\xi^{t,(\pm1)}_{\pm1}\psi^{(\pm1)}_{\pm1} + \xi^r_{\pm1}\psi^{(\pm1)}_{\pm1}}. \tag{45b}$$

We can now write the field in the time domain. We use the following relation:

$$E^r(t) = \sum_{n=-N}^{N} \big|\tilde{E}^r_n\big| \cos\big(\omega_n t + \varphi^r_n\big), \tag{46}$$

where $\varphi^r_n = \angle\tilde{E}^r_n$ is the phase of E^r_n. In Fig. 4(a) we can see the reflected field from the interface for the fast modulation case with $\Omega/\omega^0 = 0.1$, at the critical angle of the nominal stationary medium as a function of time. This angle is particularly interesting, because of the relatively high change of amplitude expected as a function of time. We notice that there is a clear difference in the reflection behavior in this fast-modulation case compared to the slow quasistatic modulation that is shown in Fig. 3. Here, the transition from regular reflection to total reflection seems a little blurry, with the reflection coefficients that are closer to one even at the lowest picks and can even momentary pass it at the higher ones. We see excellent agreement between the analytical approximation to the numerical calculation for $N = 1$ and 2. The same agreement is shown in Fig. 4(b) for a different incidence angle, away from the critical angle, and with faster modulation. This case will be further discussed below.

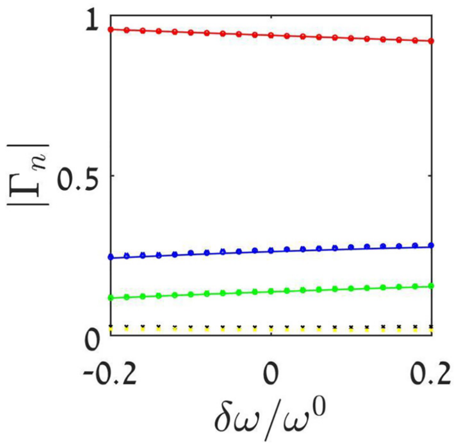

FIG. 5. Harmonics absolute values. Continuous line, analytic approximation; o-mark, numerical calculation with $N = 1$; x-mark, numerical calculation with $N = 2$. Red, $|E^r_0|$; blue, $|E^r_{-1}|$; green, $|E^r_1|$; black, $|E^r_{-2}|$; yellow, $|E^r_2|$.

The variance in the amplitude of the reflected field depends on the amplitude of the harmonics. As we can see, in Fig. 5, harmonics $n = \pm2$ are much weaker than $n = \pm1$. Let us define the harmonic energy ratio HER with

$$\mathrm{HER} = \frac{\big|\tilde{E}^r_{-1}\big|^2 + \big|\tilde{E}^r_1\big|^2}{\big|\tilde{E}^r_{-1}\big|^2 + \big|\tilde{E}^r_0\big|^2 + \big|\tilde{E}^r_1\big|^2}. \tag{47}$$

The harmonic energy ratio is a function of both the modulation frequency Ω and the incident angle θ_i. In Fig. 6 we can see this ratio, and notice an interesting dependence, that indicates that the higher the modulation frequency, the lower the incident angle that brings the maximum harmonic energy ratio HER. We also note that for small modulation frequencies (but one that is still considered "fast" by our definition), we get the maximum value of HER near the critical angle. Away from the critical angle, the required modulation frequency increases

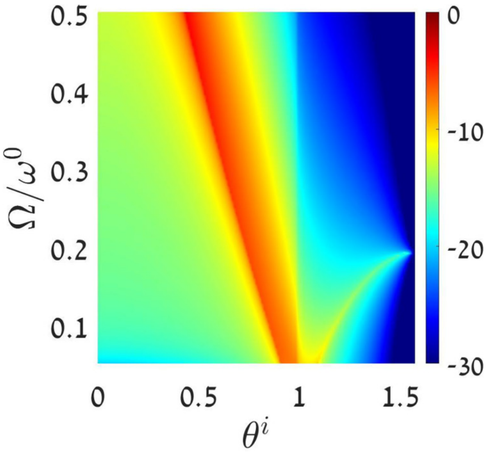

FIG. 6. The harmonic energy ratio HER (dB) between the energy of the harmonics and the total reflected energy as a function of the incident angle and modulation frequency, with modulation depth $m = 0.2$. Near the critical angle (here at $\theta_i = 0.99$) the ratio decreases fast when increasing the modulation speed.

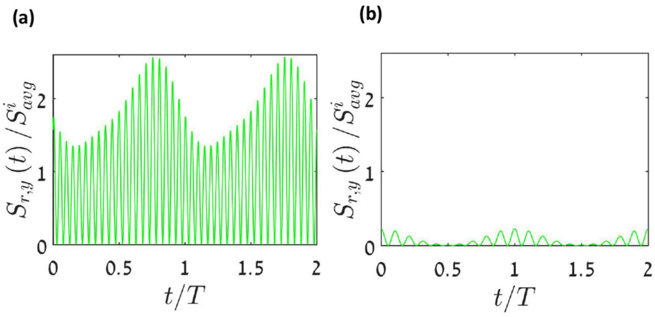

FIG. 7. Analytical approximation of the reflected y component of the momentary Poynting vector, normalized with the average incident y component of the Poynting vector. (a) $\theta^i = \theta^i_c = 0.99$ rad and $\Omega/\omega^0 = 0.1$; (b) $\theta^i = 0.73$ and $\Omega/\omega^0 = 0.2$.

[see Fig. 4(b), which shows the reflected field with maximal HER at $\Omega/\omega^0 = 0.2$ and $\theta^i = 0.73$ rad].

It is also interesting to examine the energy density balance in this case. We focus on the perpendicular to the surface component of the Poynting vector, i.e., the y component. The average incident y component of the Poynting vector satisfies

$$S^i_{\mathrm{avg},y} = \frac{1}{2\eta}|\tilde{E}^i|^2 \cos\theta^i. \tag{48}$$

The momentarily reflected y component of the Poynting vector reads

$$S^r_y(t) = \frac{1}{\eta}\left[\sum_{n=-N}^{N} \left|\tilde{E}^r_n\right| \cos\left(\omega_n t + \varphi^r_n\right)\right] \times \left[\sum_{n=-N}^{N} \cos\theta^r_n \left|\tilde{E}^r_n\right| \cos\left(\omega_n t + \varphi^r_n\right)\right]. \tag{49}$$

By averaging a sufficiently long interval of time, one obtains

$$S^r_{\mathrm{avg},y} = \frac{1}{2\eta}\sum_{n=-N}^{N} \left|\tilde{E}^r_n\right|^2 \cos\theta^r_n. \tag{50}$$

In the case, $\theta^i = \theta^c_i$ the reflected average y component of the Poynting vector is a little bit smaller than the incident y component of the Poynting vector, $S^r_{\mathrm{avg},y}/S^i_{\mathrm{avg},y} = 0.95$. This value is much higher than the slow quasistatic case, in which for an incident angle that satisfies $\theta^i = \theta^c_i$, the ratio is $S^r_{\mathrm{avg},y}/S^i_{\mathrm{avg},y} = 0.63$. (Here we average over a complete time cycle of the slow quasistatic modulation.) In Fig. 7 we bring the y component of the momentarily reflected Poynting vector normalized to the average incident Poynting vector, for both pairs of θ^i, Ω/ω^0. As expected, for the case when the incident angle equals the static critical angle [Fig. 7(a)], we can see momentarily values that surpass the value of twice the incident Poynting vector. We notice that the y component of the momentarily Poynting vector in Fig. 7(a) has an interesting asymmetrical envelope. The explanation for this behavior relies on the cross elements in Eq. (49). We also note that each harmonic has a different reflection angle [Eq. (27)], and hence is projected differently over the y component. Lastly, we note that momentarily, perpendicular to the interface, the reflected power exceeds the impinging power. This indicates some form of instantaneous amplification due to time modulation. However, as we observed numerically by calculating the expression in Eq. (50) on average the reflected power is smaller than the impinging power. This is a result of the relatively slow modulation frequency, obviously for faster modulation frequencies close to twice the impinging wave frequency strong parametric effects, and power amplification are prone to occur.

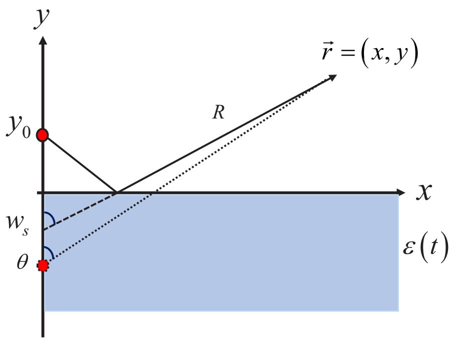

FIG. 8. The polar coordinate system.

IV. EXCITATION BY A LOCALIZED SOURCE—THE 2D GREEN'S FUNCTION

In this section, our objective is to calculate the 2D Green's function above the time-variant dielectric half-space for the case of fast modulation, and we derive a spectral integral representation for it (see Fig. 8). To accomplish this, we first decompose the line source field into a spectrum of plane waves. Subsequently, each of these plane waves interacts with the medium using the theory derived in previous sections. This enables us to write the reflected field as a spectral integral in space and summation in time. Lastly, we asymptotically evaluate the resulting spectral representation and extract insights regarding the different wave constituents propagating in this particular medium.

A. Spectral representation and the source field

We assume that a line source is located above the dielectric surface at $x = 0,\ y = y_0$. The current density of the line source can be expressed formally by $\vec{J} = \hat{z} I_s \delta(x)\delta(y - y_0)$, where δ denotes the Dirac's delta function. We utilize the theory of electromagnetic wave propagation in plane-stratified media to analyze this excitation problem. This can be done since the problem is shift-invariant to the plane normal to the y coordinate. With a straightforward calculation (see [63], Chap. 5), we get the spectral electric field due to the source when located in free space,

$$\hat{E}_z = \frac{\omega\mu I_s e^{-jk_y|y-y_0|}}{2\sqrt{2\pi}k_y}. \tag{51}$$

This field consists of a superposition of weighted plane waves, propagating and evanescent. Each of these interacts with the time-modulated lower half-space, according to the reflection formulation we derived in the former sections, thus composing the spectral representation for the reflected Green's function. This is done below.

B. Spectral representation of the reflected field

Equation (51) provides the spectral plane wave amplitudes required to construct the line source field. Using the linearity of the problem, we can cast the scattered field of the time-modulated permittivity by applying the scattering theory developed in the previous sections for each of the impinging plane waves that construct the source field. Then, we will integrate the spectral parameter to go back to the physical space domain. By Eq. (51), the impinging wave amplitude on $y = 0$, for a plane wave with spectral parameter k_0, reads

$$\hat{E}_z^i = -\frac{\omega\mu I_s}{2k_y\sqrt{2\pi}}e^{-jk_y y_0}. \tag{52}$$

Once the impinging plane wave is known, including its direction of arrival, which is encoded by the spectral parameter k_x, we can calculate the spectral reflected field with

$$\tilde{E}_n^r(\vec{r}) = \tilde{E}_z^i\Gamma_n e^{-j(k_x x+k_{n,y}y)}. \tag{53}$$

We can now directly apply the result from Eq. (53) in Eqs. (45a) and (45b) to obtain the reflected field amplitude, for the spectral parameter k_x, for any frequency harmonic n. This reads

$$\hat{E}_n^r(\vec{r}) = -\frac{k_0\eta I_s}{2k_y\sqrt{2\pi}}\Gamma_n e^{-jk_{0,y}y_0}e^{-j(k_x x+k_{n,y}y)}. \tag{54}$$

We note that the demand for continuous electric and magnetic fields over the surface leads to $k_{n,x} = k_x$. The sum over the spectral components gives us the scattered field by the 2D point source,

$$E_n^r(\vec{r}) = -\frac{k_0\eta I_s}{4\pi}\int_{-\infty}^{\infty}\frac{\Gamma_n e^{-jk_{0,y}y_0}e^{-j(k_x x+k_{n,y}y)}}{k_{0,y}}dk_x \tag{55}$$

with

$$k_{n,y} = \sqrt{k_n^2 - k_x^2}. \tag{56}$$

The expressions for $\Gamma_n(k_x)$ are given in Eqs. (45a) and (45b), with the effective velocities ξ_0^i, ξ_n^r, and $\xi_n^{t,(s)}$ given in Eq. (31), where $\cos\theta^i$ is replaced with $k_{0,y}/k_0$, $\cos\theta_n^r$ with $k_{n,y}/k_0$, and $\cos\theta^{t,(s)}$ with $\sqrt{(q^{(s)})^2 - k_x^2}/q^{(s)}$.

We now compare two different calculations to examine our analysis. We choose the following physical values values: $\varepsilon_{r0} = 0.7$, $\Omega/\omega^0 = 0.1$, $m = 0.2$, $y_0 = \lambda^0/3$. We can see in Fig. 9 good agreement between the calculations.

(i) Direct integration of Eq. (55), with the numerically calculated scattered field, via the inverse of the matrix $\underline{\underline{W}}$ for $N = 2$. To avoid singularities in our integration on the real k_x axis, we deform slightly our integration contour, with $k_x \to k_x + j\frac{2\varepsilon}{\pi}\arctan k_x$, where $\varepsilon \ll \frac{\pi}{2}k_0$ (in our case, we have chosen $\varepsilon = 0.001\frac{\pi}{2}k_0$).

(ii) Direct integration as in the previous paragraph, but with the approximated scattered field from Eqs. (45a) and (45b).

The results obtained by the aforementioned two calculation approaches are depicted in Fig. 9. A good agreement between the calculations is seen. This establishes the accuracy of the spectral representation, and in particular the approximations for the reflected fields as discussed in detail in the preceding sections. At this point, we are ready to analyze asymptotically the spectral integral. This is done in the following section.

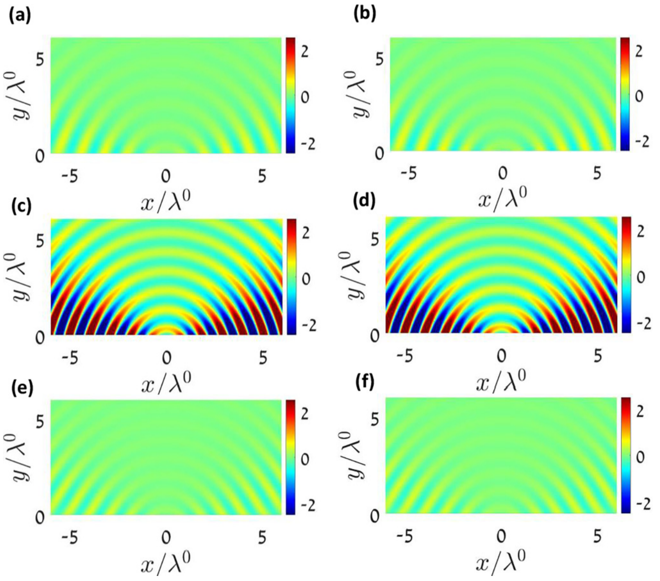

FIG. 9. The real part of the reflected electric field, normalized with the absolute value of the reflected stationary field for $n = 0$ at the origin. (a) Approximate scattered field $n = -1$, (b) accurate scattered field $n = -1$, (c) approximate scattered field $n = 0$, (d) accurate reflected field $n = 0$, (e) accurate scattered field $n = 1$, and (f) approximate scattered field $n = 1$.

C. The physical interpretation of the singular and critical points in the complex spectral plane

After confirming numerically the sufficient accuracy of the direct spectral integration over the approximate reflection coefficients in Eqs. (45a) and (45b), we can now turn to analyze the contribution of each critical point in the complex spectral plane to the different wave constituents that are excited and propagated in our system. These critical points are branch points and stationary points. There are no pole singularities in this case since no guided modes are expected in this half-space setting. We notice that there are two different types of branch points:

(i) Branch points of $k_{n,y}(k_x)$ in Eq. (56)—those branch points are located in the fast-oscillating exponent of the integrand in Eq. (55).

(ii) Branch points of $\xi_n^{t,(s)}(k_x)$—those branch points are located at the slowly varying amplitude of the integrand in Eq. (55).

This difference will be discussed in the next section. The branch points for $k_{0,y}$ can be eliminated by introducing a transformation to the complex w angle plane [63]. Specifically, we define $k_x(w) = k_0\sin w$. Then, $k_{0,y} = k_0\cos w$, and it contains no branch point in the complex w plane. Under this transformation, the integration path termed the Sommerfeld Integration Path (SIP) takes the form shown in Fig. 10. Let us now define the following polar coordinates transform: $x = R\sin\theta$, $y = R\cos\theta - y_0$, where θ is the angle of specular reflection by a stationary uniform impedance surface, i.e., if

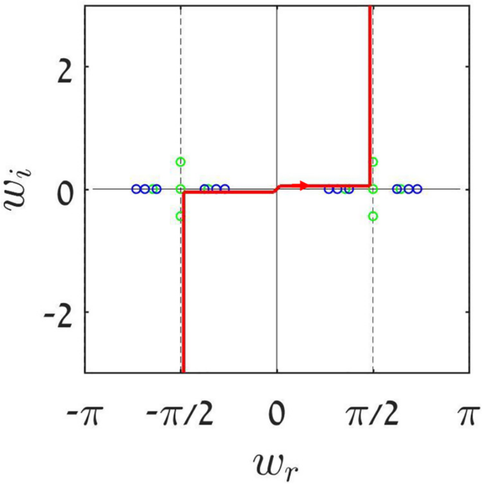

FIG. 10. The complex angle plane w. The Sommerfeld Integration Path (SIP) is shown by the red line. The branch points, shown by green circles (of $k_{n,y}$) and blue circles (of $\xi_n^{t,(s)}$), are different in their location. $k_{n,y}$ is in $p(w)$, the phase of the integral in Eq. (57), and $\xi_n^{t,(s)}$ is in $f(w)$, the spectral reflection coefficient.

the angle of incidence is equal to the angle of reflection (see the illustration in Fig. 8). We can now write the integral in Eq. (55) as

$$E_n^r(\vec{r}) = -\frac{k_0\eta I_s}{4\pi}\int_{\mathrm{SIP}}\Gamma_n(w)e^{-jp(w)}dw, \tag{57}$$

where the phase term reads

$$p(w) = k_{0,y}(w)y_0 + k_x(w)x + k_{n,y}(w)y. \tag{58}$$

In Eq. (57), the phase $p(w)$ and the amplitude which is proportional to $\Gamma_n(w)$ are assumed to be slowly varying functions in the complex integration variable w. To explore the analytic properties of the integral, we first have to identify the singular points of the integrated, which in our case are branch points only.

We start by identifying the branch points. As mentioned earlier, we are facing two types of branch points, which need different treatments:

(i) Branch points in $\Gamma_n(w)$. Those branch points can be found with the demand for nullifying $\xi_n^{t,(s)}(w)$. The branch points are $w = \arcsin\frac{q^{(s)}}{k_0}$, $w = \pi - \arcsin\frac{q^{(s)}}{k_0}$, $w = -\arcsin\frac{q^{(s)}}{k_0}$, $w = -\pi + \arcsin\frac{q^{(s)}}{k_0}$. With the specific parameters we consider in this section, the branch points are ± 0.85, ± 2.29 for $s = -1$, ± 0.99, ± 2.15 for $s = 0$, and ± 1.18, ± 1.96 for $s = 1$.

(ii) Branch point in $p(w)$. These branch points can be found with the demand for nullifying $k_{n,y}(w)$, and force us to define the branch cuts such that the SDP is continuous. The branch points are $w = \arcsin\frac{k_n}{k_0}$, $w = \pi - \arcsin\frac{k_n}{k_0}$, $w = -\arcsin\frac{k_n}{k_0}$, $w = -\pi + \arcsin\frac{k_n}{k_0}$. With the parameters considered here, the branch points are ± 1.12, 2.02 for $n = -1$, $\pm\frac{\pi}{2}$ for $n = 0$ (this is an intuitive result, since for $n = 0$ we have $\sin w_b = 1$), and $\pm\frac{\pi}{2} \pm 0.44$ for $n = 1$.

We now aim to find the saddle point w_s of the integrand in Eq. (57). At the saddle point, the phase derivative to the spectral variable nullifies, i.e., we demand $p'(w_s) = 0$, where

$$p' = -k_0y_0\sin w + k_0x\cos w - \frac{k_0^2y\sin w\cos w}{\sqrt{k_n^2 - k_0^2\sin^2 w}}. \tag{59}$$

The form of the phase term $p(w)$ is essentially similar to that typically obtained in Green's function representation in stationary layered media problems, and thus it involves a single and real saddle (stationary point) point that nullifies p' in Eq. (59). This can be shown, for example, by applying simply the intermediate value theorem in the k_x range where the phase is real.

For the case in which we are far from the saddle point value that nullifies the square root of Eq. (59), we can approximate the saddle point using the assumption of small bias δw from the specular angle θ. To that end, we first assume a small correction over the specular reflection angle, i.e., $w_s = \theta + \delta w_s$. Next we use the following Taylor approximations: $\sin(\theta + \delta w) \approx \sin\theta + \delta w\cos\theta$, $\cos(\theta + \delta w) \approx \cos\theta - \delta w\sin\theta$. Clearly, for $n = 0$, $\delta w_s = 0$. We follow the method from [43] and write the spectral wave-vector components, with second-order Taylor expansion, to easily calculate the stationary point. We get the small bias from the specular angle for the resonance harmonic,

$$\delta w_{s,n} = \frac{\left[y_0\sin\theta - \frac{1}{2}R\sin 2\theta + \frac{k_0\sin 2\theta}{2\sqrt{k_n^2 - k_0^2\sin^2\theta}}(R\cos\theta - y_0)\right]}{\left\{-y_0\cos\theta - R\sin^2\theta - \left[\frac{k_0\cos 2\theta}{\sqrt{k_n^2 - k_0^2\sin^2\theta}} + \frac{k_0^3\sin 2\theta}{2\left(k_n^2 - k_0^2\sin^2\theta\right)^{\frac{3}{2}}}\right](R\cos\theta - y_0)\right\}}. \tag{60}$$

Clearly, for the nominal frequency, there is no bias as evidenced by the fact that the numerator nullifies for $n = 0$. We further note that the expression for δw_s in Eq. (60) is valid only for specular angles θ that are not grazing the surface, with a notable difference between the different harmonics, as we can see in Fig. 11. In the case of $n = 1$, larger θ leads to somewhat less accurate results, while in the case of $n = -1$, those angles lead to complex δw_s, which has no physical meaning since it is an artifact of the approximated equation (as stated previously, there exists a real value stationary point). We note that since in our setup there is no spatial modulation, $\delta w_{s,n}$ needs to be an odd function for every n (we measure the incident angle relative to the y axis).

In the following numerical calculations for the Green's function, despite having the approximation for the saddle point location in Eq. (60), we solve numerically the equation $p'(w_s) = 0$ to avoid unnecessary approximations. Nevertheless, the approximation in Eq. (60) is of importance since it highlights quantitatively important physical observations. In asymptotic terms, the saddle point provides the angle of the

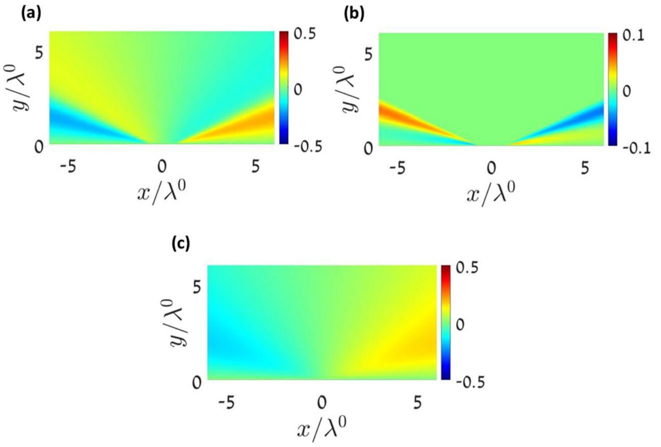

FIG. 11. δw_s for every x, y. We can see the difference in behavior for the positive and negative harmonics. (a) $\mathrm{Re}\{\delta w_{s,-1}\}$, (b) $\mathrm{Im}\{\delta w_{s,-1}\}$, (c) $\mathrm{Re}\{\delta w_{s,+1}\}$. The angle bias for the positive harmonic is purely real for all the observation angles. Both negative and positive harmonics allow us to use the approximation of small bias from the specular angle far from the grazing angles of observation but with a difference between them. While the positive harmonic leads to somewhat inaccurate results for the grazing angles, the negative harmonic leads to nonphysical complex angle bias results for those angles.

ray that leaves the source, impinges the reflecting layer, and approaches the observer. Once the saddle point is known, we seek next to find the steepest descent path (SDP), along which the integrand is not oscillatory; instead, it is monotonically increasing up to a maximal value at the saddle point and then monotonically decreasing to zero, passing between two valleys in the complex w plane. This will be useful in the numerical calculation of the deflected ray field that travels from the sources, hits the discontinuity surface, and is reflected to the observer. To find the SDP, we follow the standard recipe that is described, for example, in [63] for a phase term with a single isolated saddle point. On the SDP, by the definition, $p(w) = p(w_s) - js^2$, with $s \in (-\infty, \infty)$ denoting a real variable along the path. As s goes from $-\infty$ to ∞, the integrand in Eq. (57) exhibits essentially Gaussian behavior, with a fast decaying integrand away from the saddle (stationary) point.

The different SDP trajectories for each harmonic give rise to interesting phenomena in the complex plane, since for a large range of values of specular angles θ, each SDP encircles different branch points. To demonstrate that, we shall now explore three different observation point locations in space. We note that unlike in [43], here the effect is symmetric since there is no spatial modulation, and therefore no synthetic motion. These observation points in Cartesian coordinates (see Fig. 8) are normalized with respect to the wavelength λ^0, i.e., $(x, y)/\lambda^0$:

$$[\mathrm{a}] = (3, 4.5)\lambda^0,$$
$$[\mathrm{b}] = (3,\ 1.5)\lambda^0,$$
$$[\mathrm{c}] = (6,\ 0.25)\lambda^0.$$

For each observation point, we calculate the total spectral integral, as well as the isolated integration components by which it is composed, i.e., an integration along the SDP, and integration around the branch cuts. In Fig. 12 we bring the map of the integration path and the singular points.

The phase term for the reflected wave may contain branch-point singularities in the complex plane of the angle w. Nevertheless, the SDP should remain continuous. Otherwise, Cauchy's principle that is used to connect the SDP integration and the branch cut integrations with the original SIP integral will not be applicable. To address this issue, we uniquely define the branch cut of $k_{n,y}(w)$ such that the square root results in either a positive or negative real part in the upper Riemann sheet, in a manner that the SDP will not cross the branch cut trajectories for those branch cuts. Since the branch cuts for $\xi_n^{t,(s)}(w)$ do not affect the phase of the integral (and therefore do not affect the SDP trajectory), those branch cuts can be crossed by the SDP. We use this property to ease our analysis and define the branch cuts of $\xi_n^{t,(s)}$ the same way for every observation angle. This is demonstrated in Fig. 12, where the SDP trajectories are shown with the singular points on the complex w plane. We first note in Fig. 12(a) that no branch cut crossing is required by the SDP deformation, which implies that the SDP integral strictly equals the SIP integral (see

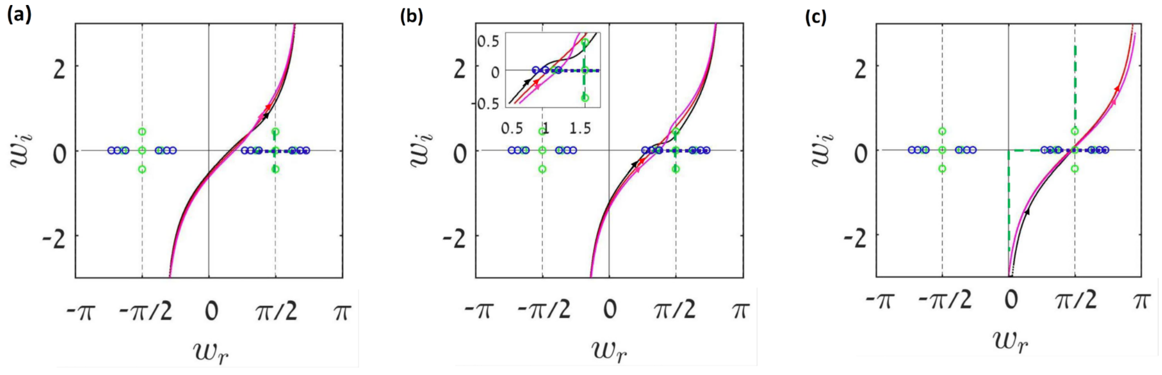

FIG. 12. The complex plane, including the SDP, and branch points, in the complex plane for three observation points listed by [a]–[c] in the text. Blue circles and the dotted blue line represent branch points and cuts of $\xi_n^{t,(s)}(w)$, and green circles and dashed lines represent branch points and cuts of $k_{n,y}(w)$. The SDP trajectories of the harmonics are as follows: black, $n = -1$; red, $n = 0$; and magenta, $n = 1$. In the inset of [b] we show the zoom-in of the SDP trajectories, of each harmonic, and we point out that each of them encircles different branch points.

TABLE I. Comparison of the exact integral calculation to the sum of the SDP and branch cuts contributions.

Observ. point and harmonic	Direct	SDP	Branch cut	Relative error
[a], $n = -1$	$-3.4\ -0.9$j	$-3.4\ -0.9$j		0
[a], $n = 0$	34.7+2j	34.7+2j		0
[a], $n = 1$	$-4.5 + 0.2$j	$-4.5 + 0.2$j		0
[b], $n = -1$	$-13.7 - 3$j	$-6.1 - 0.97$j	$-7.3 - 1.7$j	0.03
[b], $n = 0$	26.1+114.3j	26.5+91j	0.6+22.1j	0.01
[b], $n = 1$	$16.4 - 0.5$j	$-7.6 + 3.8$j	$23.7 - 4.4$j	0.02
[c], $n = -1$	$-25 - 20.2$j	3.1+0.5j	$-28 - 20.5$j	0
[c], $n = 0$	305.5+20.4j	107.1+135.6j	$192.8 - 120.1$j	0.02
[c], $n = 1$	25.7+8.6j	$4.1 -$ j	21.7+9.7j	0

Table I). T1We also note that although it seems that the SDP trajectory of the $n = -1$ harmonic crosses the branch cut of p for observation point [b] [see the black line in Fig. 12(b)], this branch cut represents $k_{1,y}(w)$, which influences only the SDP trajectory of the $n = 1$ harmonic. It is important to note that either way we choose to define the Riemann sheet, it does not affect our need to take its contribution into account, but only the integration path needed. For the observation point [b], we notice an interesting phenomenon, where each of the SDP trajectories encircles different branch points. In Figs. 13–16 we show the phase of the $k_{n,y}(w)$ for the observation points in cases [b] and [c], and the numerical path of the branch cut integration. In the insets of Figs. 13 and 14 we show the zoom-in of the SDP trajectories and the branch cuts for case [b]. We can see that the SDP trajectory is never passing through the discontinuity of the phase of the corresponding $k_{n,y}(w)$.

In Table I we present a numerical comparison between the direct numerical solution of the integral in Eq. (57), where the reflected field is calculated by Eqs. (45a) and (45b), and the sum of the isolated components: SDP integral and branch cut integral. We can see a very good agreement between the two calculations, as is evident by the error obtained when summing up the two contributions—SDP and branch cuts—to the direct spectral integration.

D. Time domain behavior

In this section, we examine the scattered field in the time domain, with an emphasis on the critical points in the complex plane. As we previously noticed in Table I, for observation points [b] and [c] the branch cut contribution is significant, and therefore it is interesting to separate the time domain scattered field into the two contributions. For each component, the time domain field can be calculated with

$$E^r(t) = \sum_{n=-1}^{1} |E_n^r| \cos\left(\omega_n t + \angle E_n^r\right). \tag{61}$$

The time domain scattered field is given in Fig. 17 for observation points [b] and [c]. To further analyze the behavior of the different wave components, we introduce an additional observation point [d] that is located at a larger distance from the source: $[d] = (20, 0.5)\lambda^0$. As expected, when the observation angle grows further from the angle where the specular angle meets the total reflection angle [b] to the observation angle [c], the more dominant the branch cut contribution is compared to

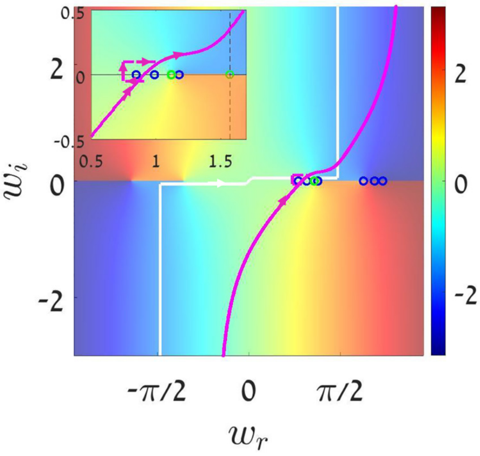

FIG. 13. Phase of $k_{-1,y}(w)$ and integration path of the branch cut numerical integration, angle [b]. Green circles represent the branch points of $k_{n,y}(w)$ and blue circles represent the branch points of $\xi_n^{t,(s)}(w)$.

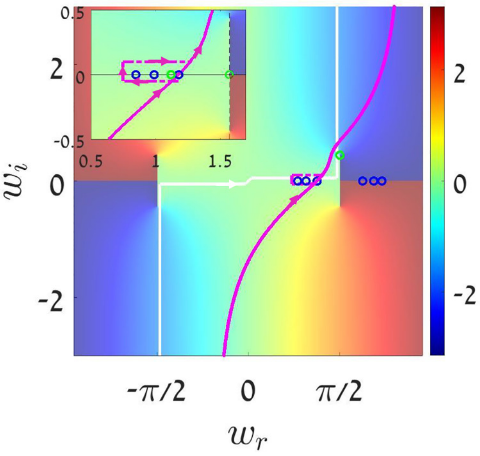

FIG. 14. Phase of $k_{1,y}(w)$ and integration path of the branch cut numerical integration - angle [b]. Green circles represent the branch points of $k_{n,y}(w)$ and blue circles represent the branch points of $\xi_n^{t,(s)}(w)$.

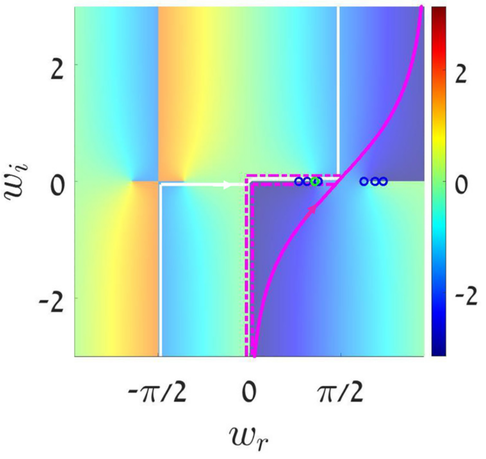

FIG. 15. Phase of $k_{-1,y}(w)$ and integration path of the branch cut numerical integration, angle [c]. Green circles represent the branch points of $k_{n,y}(w)$ and blue circles represent the branch points of $\xi_n^{t,(s)}(w)$.

the SDP contribution [see Figs. 17(a) and 17(b)]. This behavior continues until the distance becomes significantly larger (observation angle [d]), when the shading energy upward of the lateral waves leads to a faster attenuation and therefore a smaller contribution of the branch cut compared to the SDP contribution [see Fig. 17(c)]. We note an interesting behavior for observation point [b], where each harmonic crosses the branch cut differently [see Fig. 12(b)]. In particular, since the SDP trajectory of $n = 1$ crosses the branch cut further from the branch point compared to the SDP trajectory of $n = 0$, it has the same order of branch cut contribution despite the small perturbation ($m \ll 1$), as we can see in Table I. This phenomenon leads to a large variance in the envelope of the lateral wave behavior in the time domain, as we can see in Fig. 17(a). This can be interpreted as a turn "on" and "off" behavior of the lateral waves, depending on the instantaneous value of the refractive index, as expected in the adiabatic picture of the process.

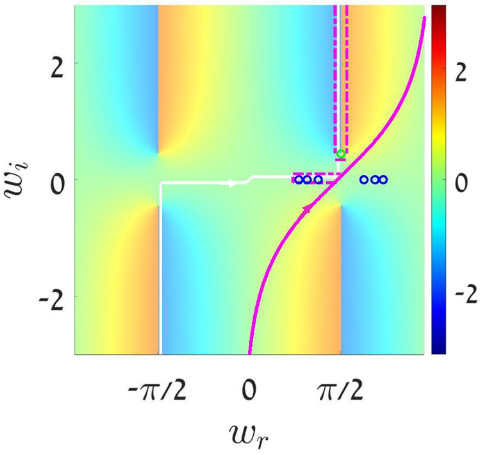

FIG. 16. Phase of $k_{1,y}(w)$ and integration path of the branch cut numerical integration, angle [c]. Green circles represent the branch points of $k_{n,y}(w)$ and blue circles represent the branch points of $\xi_n^{t,(s)}(w)$.

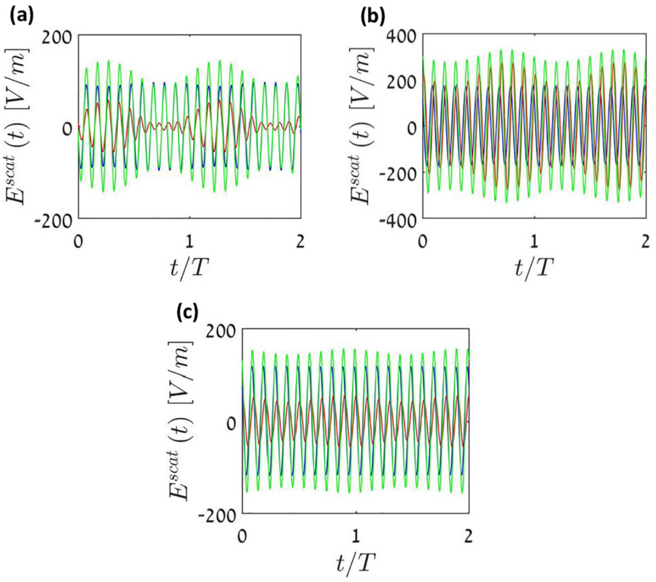

FIG. 17. The time domain scattered field. Blue, SDP contribution; red, branch cut contribution; green, total field. (a) Observation point [b], (b) observation point [c], and (c) observation point [d].

E. Asymptotic evaluation

In this section, we asymptotically evaluate the spectral representations from the previous section and discuss their limitations. We focus on the SDP integral only since the branch-cut contributions have cumbersome expressions, which are not very useful for gaining physical insight into the scattered field dynamic. We follow the method from [43], and use the asymptotic evaluation of integrals along the steepest descent paths (SDPs) [63]. For the integral Eq. (57) in the complex plane with $|q\psi| \gg 1$, the SDP contribution can be approximated with

$$E^r_{n,\mathrm{SDP}} \approx \frac{-k\eta I_s}{4\pi} e^{-j\frac{\pi}{4}} \sqrt{\frac{2\pi}{\psi q''(w_{s,n})}}\,\Gamma_n(w_{s,n}) e^{-j\psi q(w_{s,n})}, \qquad (62)$$

where $w_{s,n} = \theta + \delta w_{s,n}$ is the saddle point. We note that this approximation assumes that Γ_n is slowly varying near the saddle point, which is true only far from the singularities in the complex plane. Therefore, this approximation is only valid for large enough θ. Then, it can be shown that the second-order derivative of $p''(w_{s,n})$ can be replaced by $p''(\theta)$ with no significant loss in accuracy.

When comparing the results from Table I for observation point [a] for $n = -1$, which represents high θ, we get a relative error of 0.11. Although this relative accuracy seems somewhat moderate, it can be explained by the asymptotic behavior of Eq. (62). When increasing the distance for the observer R ($R \rightarrow 4R$), but staying at the same observation angle θ, the relative error reduces to 0.03.

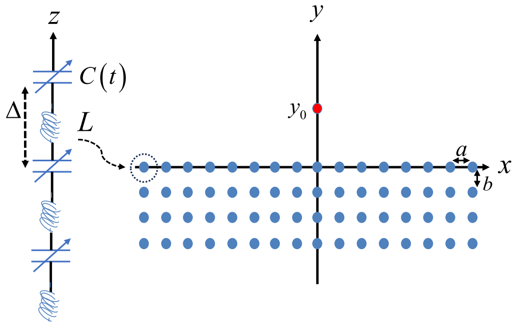

FIG. 18. Time variant modulated half-space wire medium. The wire media consist of a finite array of 301 (in width) over 151 (in height) loaded infinite wires. The actual realization of such an infinite wire can be obtained by placing a single period between the two plates of a parallel plates waveguide. Then, an array of "wires" can be built accordingly (see, e.g., [60], Sec. 5.5.4).

V. APPROXIMATE HOMOGENIZATION OF TEMPORALLY MODULATED WIRE MEDIUM

In this section, we implement the theory from the previous sections and suggest a realization of the time-modulated half-space that is based on the homogenization of a temporally modulated wire medium (see Fig. 18). We follow the homogenization approach from [16], with two notable differences—here we are not necessarily at the close environment of the plasma frequency, and there is no spatial modulation. Assume that the loading capacitance on each of the wires is modulated as

$$C(t) = C_0(1 + m_c \cos \Omega t), \qquad m_c \ll 1. \tag{63}$$

To be able to calculate the effective properties of the medium, and implement the homogenization, we need to demand a dense grid, i.e., $ka, kb \ll 1$, which eliminates the propagation of high-order Floquet modes. We choose the following physical parameters: $a = 0.1\lambda_0,\ b = 0.1\lambda_0,\ r_0 = 0.0001\lambda_0$. In this case, the recursive matrix elements read

$$a_n = c_n = \frac{m_c}{2\omega_n \tilde{C}}, \tag{64a}$$

$$b_n = \omega_n \tilde{L} - \frac{1}{\omega_n \tilde{C}} - \frac{\eta k_n}{ab\left(k_n^2 - q^2\right)}, \tag{64b}$$

where $\tilde{C} = C_0\Delta$ and $\tilde{L} = \tilde{L}_w + \tilde{L}_0$, $\tilde{L}_0 = L_0/\Delta$, with

$$\tilde{L}_w = \frac{\eta}{2c}\left(\frac{1}{\pi}\ln\frac{b}{2\pi r_0} + \sum_{l=1}^{\infty}\frac{\coth\left(\pi a l/b\right) - 1}{\pi l} + \frac{a}{6b}\right), \tag{65}$$

where L_0 is an inductance that may be connected in series with the loading capacitor $C(t)$. Effectively it simply increases the intrinsic wire inductance. The relation between the static permittivity and the physical characteristics of the medium is

$$\varepsilon_{r0} = 1 - \frac{\eta}{abk_0\left(\omega_0\tilde{L} - \frac{1}{\omega_0\tilde{C}}\right)}. \tag{66}$$

To estimate the relation between the perturbation m of the effective medium and the perturbation of the capacitance m_c, we can plug $\tilde{C} = \Delta C(t)$ in Eq. (66) and make a first-order

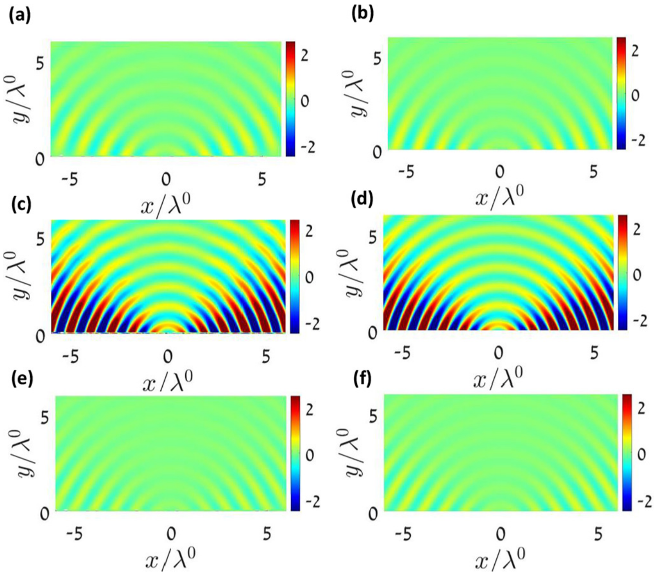

FIG. 19. The real part of the scattered electric field, normalized with the absolute value of the scattered stationary field for $n = 0$ at the origin. (a) Wire medium scattered field $n = -1$, (b) effective medium scattered field $n = -1$, (c) wire medium scattered field $n = 0$, (d) effective medium scattered field $n = 0$, (e) effective medium scattered field $n = 1$, and (f) wire medium scattered field $n = 1$.

approximation,

$$\varepsilon_{r0}(t) \approx 1 - \frac{\eta}{abk_0\left(\omega_0\tilde{L} - \frac{1}{\omega_0\tilde{C}}\right)} + \frac{\eta m_c \cos\Omega t}{abk_0\omega_0\tilde{C}\left(\omega_0\tilde{L} - \frac{1}{\omega_0\tilde{C}}\right)^2}. \tag{67}$$

We can now compare the elements from Eq. (67) with the expression from Eq. (4), and get the relation

$$m = \frac{\eta m_c}{abk_0\omega_0\tilde{C}(\varepsilon_{r0} - 1)\left(\omega_0\tilde{L} - \frac{1}{\omega_0\tilde{C}}\right)^2}. \tag{68}$$

As explained in detail in [16], the processes of homogenization and temporal modulation are not entirely interchangeable. Indeed, when calculating the irregular eigenmodes of the temporal wire medium, we get a slight bias from the irregular modes of the homogenized medium (see Appendix C). The regular modes of both media are close to equal since we demand a matching effective permittivity. In our case ($\varepsilon_{r0} = 0.7$, $m = 0.2$), the equivalent physical parameters are $L_0 = 0.5\,\mu\text{H}$, $C_0 = 0.12\,\text{pF}$, $\Delta = 0.1\lambda_0$. The capacitance perturbation is $m_c = -0.3$. In Fig. 19 we present a comparison between the numerical quasifrequency domain simulation of the scattered field from a finite-size wire medium (301 wires over the x axis and 151 wires over the y axis). The boundary of the wire medium contains a small amount of gradual loss to reduce the effect of scattering and diffraction from the edges and corners of the medium and the calculation of the effective temporally modulated dielectric (this calculation is the same one as in Fig. 9, from the approximate integration). As expected, we get a good (but not exact) agreement between the numerical simulation and the calculation of the homogenized medium. The major difference between the wire medium and the homogenized medium is the fact that the wire medium is highly dispersive, while the dielectric model assumed in this paper is instantaneous—and hence nondispersive. In addition, we note that the processes of homogenization and temporal modulation are not entirely interchangeable [16], and therefore the two problems lead to some differences in the irregular modes. These differences need to be added to the fact that higher Floquet modes are not completely negligible, hence the moderate differences between the analytical homogenization calculation to the numerical simulation of the wire medium.

VI. CONCLUSIONS AND OUTLOOK

In this paper, we have developed a rigorous excitation theory for time-modulated dielectric infinite half-space. The theory enables the derivation of the separated wave components that comprise the Green's function. From a mathematical standpoint, these are related to different singularities and unique points in the complex spectral plane. Although here for the sake of concreteness we considered the Green's function due to a source above a discontinuity, the theory can be applied to various excitation scenarios, such as the excitation of a multilayered modulated media. The advantage of having a Green's function is twofold: from the physical perspective, it provides a deeper understanding of the wave problem, while from the numerical perspective it may be useful in numerical schemes based on integral equations for the excitation and propagation in time-modulated media. Lastly, we implement the suggested technique on a homogenized temporally modulated wire medium and identify the strengths and limitations of this technique.

ACKNOWLEDGMENT

This research was supported by the Israel Science Foundation (Grant No. 1457/23).

APPENDIX A: THE RELATION BETWEEN THE TIME-HARMONICS OF THE ELECTRIC FIELD

We aim to formulate the relation between the frequency harmonics in the time-variant medium. For the nth harmonic, we can write

$$\vec{\nabla} \times \vec{H}_n = \hat{z} j \varepsilon_0 \omega_n \left[\varepsilon_{r0} E_n + \frac{m}{2}(\varepsilon_{r0} - 1)(E_{n-1} + E_{n+1}) \right]. \tag{A1}$$

Since the eigenmodes are plane waves, their spatial dependence is expressed as $e^{-j\vec{q}\cdot\vec{r}}$. Then Eq. (6) can be written as

$$-\frac{1}{\varepsilon_0} j\vec{q}_n \times \vec{H}_n = \hat{z} j \omega_n \left[\varepsilon_{r0} E_n + \frac{m}{2}(\varepsilon_{r0} - 1)(E_{n-1} + E_{n+1}) \right]. \tag{A2}$$

Then from Faraday's law,

$$\hat{z} q_n^2 E_z = -j\omega_n \mu \varepsilon_0 \frac{(-j\vec{q}_n)}{\varepsilon_0} \times \vec{H}. \tag{A3}$$

The last two equations yield the following relation between the time-harmonics of the electric field:

$$\left(q_n^2 - \varepsilon_{r0} k_n^2\right) E_n = \frac{m k_n^2}{2} (\varepsilon_{r0} - 1)(E_{n-1} + E_{n+1}), \tag{A4}$$

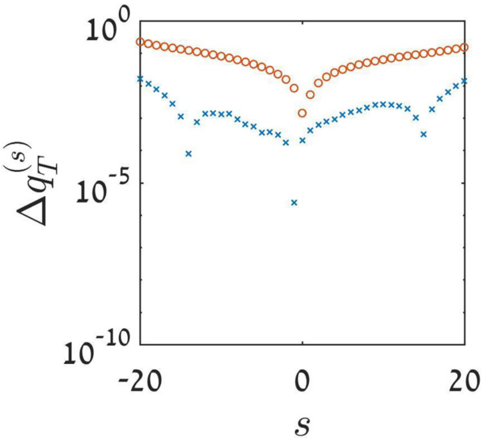

FIG. 20. Slow modulation relative error $\Delta q^{(s)}_{(T)} = |q^{(s)} - q^{(s)}_{(T)}|/|q^{(s)}_{(T)}|$ between the direct calculation of the wave-number modes for $N = 20$ to the approximate Toeplitz calculation from Eq. (16). "x" marks represent $\frac{\Omega}{\omega^0} = 0.001$, and "o" marks represent $\frac{\Omega}{\omega^0} = 0.01$. $q_T^{(s)}$ represent the approximate Toeplitz modes, and $q^{(s)}$ represent the direct calculation modes.

where $k_n = \omega_n / c$. Equation (A4) holds for every observation point $\vec{r}$ in the medium. Since the eigenfields are plane waves, we can write the following relation: $E_n = \tilde{E}_n e^{-j\vec{q}_n\cdot\vec{r}}$, where $\tilde{E}_n$ is the field amplitude. Combining both these statements gives us the following momentum conservation relation: $q = q_n = q_{n+1}$. Therefore, Eq. (A4) can be now written without the index n for q,

$$\left(q^2 - \varepsilon_{r0} k_n^2\right) E_n = \frac{m k_n^2}{2} (\varepsilon_{r0} - 1)(E_{n-1} + E_{n+1}). \tag{A5}$$

APPENDIX B: SLOW QUASISTATIC MODULATION EIGENVALUES

When analyzing the effect of the frequency modulating, we need to take into account the case of a very slow modulation, i.e., $O(\frac{\Omega}{\omega}) \ll O(m^2)$. In this case, the matrix in Eq. (10a) cannot be truncated. In Eqs. (15a) and (15b), we show the matrix elements with the approximation of neglecting completely the frequency modulation, i.e., $\frac{\Omega}{\omega} \approx 0$, to be able to approximate the matrix to a Toeplitz matrix, which has a closed form for its eigenvalues. Let us examine the quality of this approximation. In Fig. 20, we can see an example for the parameters $m = 0.2$, $\varepsilon_{r0} = 0.7$ for the relative error of this approximation for two slow modulation frequencies $\frac{\Omega}{\omega} = 0.01$, $\frac{\Omega}{\omega} = 0.001$, and as expected, the slower the modulation, the lower the error of this approximation. Since we have noticed that the Toeplitz approximation is valid for small enough modulation frequency, we can now use the straight formula for the eigenmodes in Eq. (16) to choose N, with the tolerable error of the calculated modes.

APPENDIX C: WIRE MEDIUM EIGENMODES

To calculate the eigenmodes of the temporally modulated wire medium, we follow the method of [16] and write the approximate determinant of the truncated matrix with $N = 1$.

We get the following equation:

$$\frac{(m_c)^2}{4\tilde{C}^2}\left[\frac{1}{X_{-1}(\omega,q)}+\frac{1}{X_1(\omega,q)}\right]=X_0(\omega,q) \tag{C1}$$

with

$$X_n(\omega,q)=\omega_n\left[\omega_n\tilde{L}-\frac{1}{\omega_n\tilde{C}}-\frac{\eta k_n}{ab\left(k_n^2-q^2\right)}\right]. \tag{C2}$$

We can now calculate the irregular modes, in the same way that we did for the temporally modulated permittivity. In the case of zero perturbation,

$$q^{(\pm1)}(m_c=0)=\sqrt{k_{\pm1}^2-\frac{\eta k_{\pm1}}{ab\left(\omega_{\pm1}\tilde{L}-\frac{1}{\omega_{\pm1}\tilde{C}}\right)}}. \tag{C3}$$

Again, we plug in the expression for the eigenmode for the case of zero perturbation in Eq. (C1), and we get the more accurate expression for the eigenmodes. Due to the required equality for the unperturbed regular eigenmodes (to calculate the effective stationary permittivity of the medium), we expect that the bias of the irregular modes will be greater than the regular ones. The corrected expressions get the form

$$q^{(\pm1)}=\sqrt{k_{\pm1}^2-\frac{\eta k_{\pm1}}{ab\left\{\omega_{\pm1}\tilde{L}-\frac{1}{\omega_{\pm1}\tilde{C}}-\frac{1}{\omega_0\left[\frac{X_0(\omega,q^{(\pm1)}(m_c=0))}{\frac{(m_c)^2}{4\tilde{C}^2}}-\frac{1}{X_{\mp1}(\omega,q^{(\pm1)}(m_c=0))}\right]}\right\}}}, \tag{C4a}$$

$$q^{(0)}=\sqrt{k_0^2-\frac{\eta k_0}{ab\left\{\omega_0\tilde{L}-\frac{1}{\omega_0\tilde{C}}-\frac{(m_c)^2}{4\omega^0\tilde{C}^2}\left[\frac{1}{X_{-1}(\omega,q^{(0)}(m_c=0))}+\frac{1}{X_1(\omega,q^{(0)}(m_c=0))}\right]\right\}}}. \tag{C4b}$$

For the wire medium, we get the eigenmodes $q^{(-1)}=13.9$, $q^{(0)}=17.5$, $q^{(1)}=20.3$, and for the effective homogenized temporally modulated medium, we get the eigenmodes $q^{(-1)}=15.6$, $q^{(0)}=17.5$, $q^{(1)}=19.6$.

[1] R. L. Fante, Transmission of electromagnetic waves into time-varying media, IEEE Trans. Antennas Propag. **19**, 417 (1971).

[2] F. R. Morgenthaler, Velocity modulation of electromagnetic waves, IRE Trans. Microwave Theory Tech. **6**, 167 (1958).

[3] A. Akbarzadeh, N. Chamanara, and C. Caloz, Inverse prism based on temporal discontinuity and spatial dispersion, Opt. Lett. **43**, 3297 (2018).

[4] S. F. Preble, Q. Xu, and M. Lipson, Changing the colour of light in a silicon resonator, Nat. Photon. **1**, 293 (2007).

[5] D. Torrent, O. Poncelet, and J.-C. Batsale, Nonreciprocal thermal material by spatiotemporal modulation, Phys. Rev. Lett. **120**, 125501 (2018).

[6] H. Nassar, X. C. Xu, A. N. Norris, and G. L. Huang, Modulated phononic crystals: Non-reciprocal wave propagation and Willis materials, J. Mech. Phys. Solids **101**, 10 (2017).

[7] J. R. Zurita-Sánchez, P. Halevi, and J. C. Cervantes-González, Reflection and transmission of a wave incident on a slab with a time-periodic dielectric function, Phys. Rev. A **79**, 053821 (2009).

[8] J. S. Martínez-Romero, O. M. Becerra-Fuentes, and P. Halevi, Temporal photonic crystals with modulations of both permittivity and permeability, Phys. Rev. A **93**, 063813 (2016).

[9] V. Bacot, M. Labousse, A. Eddi, M. Fink, and E. Fort, Time reversal and holography with spacetime transformations, Nat. Phys. **12**, 972 (2016).

[10] S. Vezzoli, V. Bruno, C. DeVault, T. Roger, V. M. Shalaev, A. Boltasseva, M. Ferrera, M. Clerici, A. Dubietis, and D. Faccio, Optical time reversal from time-dependent Epsilon-Near-Zero media, Phys. Rev. Lett. **120**, 043902 (2018).

[11] Z.-L. Deck-Léger, A. Bahrami, Z. Li, and C. Caloz, Orthogonal analysis of space–time crystals, Opt. Lett. **48**, 4253-4256 (2023).

[12] A. Bahrami, Z.-L. Deck-Léger, and C. Caloz, Electrodynamics of accelerated-modulation space-time metamaterials, Phys. Rev. Appl. **19**, 054044 (2023).

[13] G. Lerosey, J. De Rosny, A. Tourin, A. Derode, G. Montaldo, and M. Fink, Time reversal of electromagnetic waves, Phys. Rev. Lett. **92**, 193904 (2004).

[14] V. Pacheco-Peña, Effective medium concept in temporal metamaterials, Nanophotonics **9**, 379 (2020).

[15] D. M. Solís and N. Engheta, A Generalization of the Kramers-Kronig relations for linear time-varying media, Phys. Rev. B **103**, 144303 (2021).

[16] M. Kreiczer and Y. Hadad, Wave analysis and homogenization of a spatiotemporally modulated wire medium, Phys. Rev. Appl. **16**, 054003 (2021).

[17] Y. Ayasli, Field effect transistor circulators, IEEE Trans. Magn. **25**, 3242 (1989).

[18] K. Gallo and G. Assanto, All-optical diode in a periodically poled lithium niobate waveguide, Appl. Phys. Lett. **79**, 314 (2001).

[19] T. Kodera, D. L. Sounas, and C. Caloz, Artificial Faraday rotation using a ring metamaterial structure without static magnetic eld, Appl. Phys. Lett **99**, 031114 (2011).

[20] D. L. Sounas, T. Kodera, and C. Caloz, Electromagnetic modeling of a magnetless nonreciprocal gyrotropic metasurface, IEEE Trans. Antennas Propag. **61**, 221 (2013).

[21] Z. Wang, Z. Wang, J. Wang, B. Zhang, J. Huangfu, J. D. Joannopoulos, M. Soljacic, and L. Ran, Gyrotropic response in the absence of a bias field, Proc. Natl. Acad. Sci. USA **109**, 13194 (2012).

[22] B. I. Popa and S. A. Cummer, Nonreciprocal active metamaterials, Phys. Rev. B **85**, 205101 (2012).

[23] S. Manipatruni, J. T. Robinson, and M. Lipson, Optical nonreciprocity in optomechanical structures, Phys. Rev. Lett. **102**, 213903 (2009).

[24] Y. Mazor and A. Alú, Nonreciprocal hyperbolic propagation over moving metasurfaces, Phys. Rev. B **99**, 045407 (2019).

[25] R. Fleury, D. L. Sounas, C. F. Sieck, M. R. Haberman, and A. Alú, Sound isolation and giant linear nonreciprocity in a compact acoustic circulator, Science **343**, 516 (2014).

[26] S. Qin, Q. Xu, and Y. E. Wang, Nonreciprocal components with distributedly modulated capacitors, IEEE Trans. Microwave Theor. Techn. **62**, 2260 (2014).

[27] N. Reiskarimian and H. Krishnaswamy, Magnetic-free nonreciprocity based on staggered commutation, Nat. Commun. **7**, 11217 (2016).

[28] Z. Yu and S. Fan, Complete optical isolation created by indirect interband photonic transitions, Nat. Photon. **3**, 94 (2009).

[29] H. Lira, Z. Yu, S. Fan, and M. Lipson, Electrically driven nonreciprocity induced by interband photonic transition on a silicon chip, Phys. Rev. Lett. **109**, 033901 (2012).

[30] D. L. Sounas, C. Caloz, and A. Alú, Giant non-reciprocity at the subwavelength scale using angular momentum-biased metamaterials, Nat. Commun. **4**, 2407 (2013).

[31] N. A. Estep, D. L. Sounas, J. Soric, and A. Alú, Magnetic-free non-reciprocity and isolation based on parametrically modulated coupled-resonator loops, Nat. Phys. **10**, 923 (2014).

[32] R. Sabri, M. M. Salary, and H. Mosallaei, Broadband continuous beam-steering with time-modulated metasurfaces in the near-infrared spectral regime, APL Photon. **6**, 086109 (2021).

[33] H. Li, S. Yin, and A. Alú, Nonreciprocity and Faraday rotation at time interfaces, Phys. Rev. Lett. **128**, 173901 (2022).

[34] H. He, S. Zhang, J. Qi, F. Bo, and H. Li, Faraday rotation in nonreciprocal photonic time-crystals, Appl. Phys. Lett. **122**, 051703 (2023)

[35] F. R. Prudêncio and M. G. Silveirinha, Synthetic axion response with space-time crystals, Phys. Rev. Appl. **19**, 024031 (2023).

[36] F. R. Prudêncio and M. G. Silveirinha, Replicating physical motion with Minkowskian isorefractive spacetime crystals, Nanophotonics **12**, 3007 (2023).

[37] Y. Hadad, D. L. Sounas, and A. Alu, Space-time gradient metasurfaces, Phys. Rev. B **92**, 100304(R) (2015).

[38] Y. Hadad, J. C. Soric, and A. Alú, Breaking temporal symmetries for emission and absorption, Proc. Natl. Acad. Sci. USA **113**, 3471 (2016).

[39] A. Shlivinski and Y. Hadad, Beyond the Bode-Fano bound: Wideband impedance matching for short pulses using temporal switching of transmission-line parameters, Phys. Rev. Lett. **121**, 204301 (2018).

[40] H. Li and A. Alú, Temporal switching to extend the bandwidth of thin absorbers, Optica **8**, 24 (2021)

[41] C. Firestein, A. Shlivinski, and Y. Hadad, Absorption and scattering by a temporally switched lossy layer: Going beyond the Rozanov bound, Phys. Rev. Appl. **17**, 014017 (2022)

[42] O. Silbiger and Y. Hadad, Optimization-free filter and matched-filter design through spatial and temporal soft switching of the dielectric constant, Phys. Rev. Appl. **19**, 014047 (2023)

[43] M. Kreiczer and Y. Hadad, Green's function theory of spatiotemporally modulated loaded wire surface, Phys. Rev. Res. **5**, 043256 (2023)

[44] S. I. Maslovski and M. G. Silveirinha, Nonlocal permittivity from a quasistatic model for a class of wire media, Phys. Rev. B **80**, 245101 (2009).

[45] P. A. Belov, S. A. Tretyakov, and A. J. Viitanen, Dispersion and reflection properties of artificial media formed by regular lattices of ideally conducting wires, J. Electromagn. Waves. Appl. **16**, 1153 (2002).

[46] N. A. Nicorovici, R. C. McPhedran, and L. C. Botten, Photonic bad gaps for array of perfectly conducting cylinders, Phys. Rev. E **52**, 1135 (1995).

[47] S. K. Chin, N. A. Nicorovici, and R. C. McPhedran, Green's function and lattice sums for electromagnetic scattering by a square array of cylinders, Phys. Rev. E **49**, 4590 (1994).

[48] V. Kuzmiak, A. A. Maradudin, and F. Pincemin, Photonic band structures of two dimensional systems containing metallic components, Phys. Rev. B **50**, 16835 (1994).

[49] V. Kuzmiak, A. A. Maradudin, and A. R. Mcgurn, Photonic band structures of two dimensional systems fabricated from rods of a cubic polar crystal, Phys. Rev. B **55**, 4298 (1997).

[50] K. Sakoda, Photonic bands of metallic systems I. Principle of calculation and accuracy, Phys. Rev. B **64**, 045116 (2001).

[51] M. M. Sigalas, Metallic Photonic band gap materials, Phys. Rev. B **52**, 11744 (1995).

[52] M. G. Silveirinha and S. I. Maslovski, Radiation from elementary sources in a uniaxial wire medium, Phys. Rev. B **85**, 155125 (2012).

[53] M. G. Silveirinha, Additional boundary condition for the wire medium, IEEE Trans. Antennas Propag. **54**, 1766 (2006).

[54] M. G. Silveirinha, C. A. Fernandes, and J. R. Costa, Additional boundary condition for a wire medium connected to a metallic surface, New J. Phys. **10**, 053011 (2008).

[55] M. G. Silveirinha, C. A. Fernandes, and J. R. Costa, Electromagnetic characterization of textured surfaces formed by metallic pins, IEEE Trans. Antennas Propag. **56**, 405 (2008).

[56] G. W. Hanson, E. Forati, and M. G. Silveirinha, Modeling of spatially-dispersive wire media: Transport representation, comparison with natural materials, and additional boundary conditions, IEEE Trans. Antennas Propag. **60**, 4219 (2012).

[57] E. Forati and G. W. Hanson, Scattering from isotropic connected wire medium metamaterials: Three-, two-, and one-dimensional cases, IEEE Trans. Antennas Propag. **61**, 3564 (2013).

[58] G. W. Hanson, M. G. Silveirinha, P. Burghignoli, and A. B. Yakovlev, Nonlocal susceptibility of the wire medium in the spatial domain considering material boundaries, New J. Phys. **15**, 083018 (2013).

[59] A. B. Yakovlev, M. Hedayati, M. G. Silveirinha, and G. W. Hanson, A local thickness-dependent permittivity model for non-local bounded wire-medium structures, Phys. Rev. B **94**, 155442 (2016).

[60] S. Tretyakov, *Analytical Modeling in Applied Electromagnetics* (Artech House, Boston, 2003).

[61] R. M. Gray, Toeplitz and circulant matrices: A review, Found. Trends Commun. Inf. Theor. **2**, 155 (2005).

[62] M. Born and E. Wolf, *Principles of Optic's* (Pergamon Press, New York, 1959), p. 37.

[63] L. B. Felsen and N. Marcuvits, *Radiation and Scattering of Waves*, IEEE/OUP Series on Electromagnet Wave Theory (IEEE, Piscataway, NJ, 1996).